Optimizing Fast Charging and Wetting in Lithium-Ion Batteries with Optimal Microstructure Patterns Identified by Genetic Algorithm

Francois L. E. Usseglio-Viretta,[1,z] Peter J. Weddle,[1] Bertrand J. Tremolet de Villers,[2] Nathan Dunlap,[1] Dana Kern,[2] Kandler Smith,[1] and Donal P. Finegan[1]

[1]*Center for Energy Conversion & Storage Systems, National Renewable Energy Laboratory, Golden, Colorado 80401, United States of America*
[2]*Center for Materials Science, National Renewable Energy Laboratory, Golden, Colorado 80401, United States of America*

To sustain the high-rate current required for fast charging electric vehicle batteries, electrodes must exhibit sufficiently high effective ionic diffusion. Additionally, to reduce battery manufacturing costs, wetting time must decrease. Both of these issues can be addressed by structuring the electrodes with mesoscale pore channels. However, their optimal spatial distribution, or patterns, is unknown. Herein, a genetic algorithm has been developed to identify these optimal patterns using a CPU-cheap proxy distance-based model to evaluate the impact of the added pore networks. Both coin-cell and pouch cell form factors have been considered for the wetting analysis, with their respective electrolyte infiltration mode. Regular hexagonal and mud-crack-like patterns, respectively, for fast charging and fast wetting were found to be optimal and have been compared with pre-determined, easier to manufacture, patterns. The model predicts that using cylindrical channels arranged in a regular hexagonal pattern is ∼6.25 times more efficient for fast charging as compared to grooved lines with both structuring strategies being restricted to a 5% electrode total volume loss. The model also shows that only a very limited electrode volume loss (1%–2%) is required to dramatically improve the wetting (5–20 times) compared to an unstructured electrode.

List of Symbols

			Acronym/symbol	Full name	Unit
Acronym	Battery		LIB	Lithium-ion battery	n/a
			P2D	Battery pseudo two-dimensional model	
			SOH	State of Health	
			SOP	State of Power	
			OCP	Open circuit potential	
			CC-CV	Constant current—constant voltage	
	Channel		SPN	Secondary pore network (tailored for fast charging)	n/a
			TPN	Tertiary pore network (tailored for fast wetting)	
			FOV	Field of view	
	Optimization terminology		GA	Genetic algorithm	n/a
			NSGA	Nondominated Sorting Genetic Algorithm	
			TOPSIS	Technique for Order Preference by Similarity to Ideal Solution	
	Electrode chemistry		NMC	Nickel Manganese Cobalt oxide	n/a
			$LiFePO_4$	Lithium iron phosphate	
			$LiCoO_2$	Lithium cobalt oxide	
	Imaging		SEM	Scanning electron microscopy	n/a
			EDS	Energy-dispersive X-ray spectroscopy	
Numerical methods	Objective function		pEDM	(periodic) Euclidean distance map	[m]
			$I(i, j)$	2D pixel-grid locating channels in FOV. i,j row and column subscripts.	—
			$I'(k)$	1D array indexed-based representation of I. k linear index of row and column subscripts (for SPN $I'(k)$ contains only index of disc centers). Chromosome of genetic algorithm.	—
			p	Number of pixels assigned to channel	—
			N	Number of pixels assigned to channel (cf, Eq. 4a) or number of channels (cf, Eq. 4b)	—
			N_c	Number of channels	—
			r	Channel radius	[m]

[z]E-mail: francois.usseglioviretta@nrel.gov

(Continued).

		Acronym/symbol	Full name	Unit
		f	Fitness function	[m]
		$f_{50}, f_{\min}$	Fitness function average and minimum	[m]
		$f_n, f_{50,n}, f_{\min,n}$	Normalized fitness function, normalized fitness function average and normalized fitness function minimum	[0,1]
	Genetic algorithm	POP	Population size	—
		P	Number of parents	—
		S_p	Parent selection threshold	[0,1]
		C	Number of couples	—
		C_r	Number of crossovers per couple	—
		M	Number of mutants	—
		S_m	Mutation occurrence ratio	[0,1]
		M_s	Number of mutations per mutant (mutation size)	—
	Permutation approach	n	Grid size (per direction)	—
		N	Grid size	—
		k	Number of pixels assigned to channels	—
		r	Channel surface coverage	[0,1]
Channel parameter and geometry	**SPN**. *Additional lower scripts a and c (e.g., $r_{V,a}$ for r_V) refer, respectively, to the anode and the cathode. Additional upper script p refers to the regular hexagon periodic pattern. Both can be combined, for instance $V_{c,a}^p$ for V_c*	θ_c	Channel slop	[deg]
		t_e	Electrode thickness	[m]
		t_c	Actual channel thickness	[m]
		r_t	Channel thickness ratio	[0,1]
		$t_c^{\max}$	Maximum channel thickness	[m]
		w_c^t	Channel top width	[m]
		w_c^b	Channel bottom width	[m]
		L	Periodic length (groove lines only)	[m]
		L_s	Channel spacing (edge to edge)	[m]
		L_{c-c}	Distance between nearest disc center	[m]
		r_A	Channel coverage ratio	[0,1]
		V_c^b	Bottom channel volume	[m³]
		V_c	Actual channel volume	[m³]
		$V_c^{\max}$	Maximum channel volume associated with its maximum thickness	[m³]
		r_V	Channel volume ratio	[0,1]
		$V_{e,FOV}$	Field of view volume	[m³]
		g_r	FOV number of pixel (row)	—
		g_c	FOV number of pixel (column)	—
		s	Pixel size	[m]
		FOV $V_{c,\,tot}$	Total channel volume in the FOV	[m³]
		N_c	Number of channels in the FOV	—
		C_b	Baseline capacity	[C]
		C_s	Laser structured capacity	[C]
		N/P_s	N/P ratio for the structured cell	
	TPN. *Upper script 'refers to coin cell, 'refers to pouch cell. Some parameters from SPN are re—used, with this upper script to differentiate them.*	A	Trapezoidal cross section area	[m²]
		d	Coin cell diameter (coin cell only)	[m]
		w_e	Electrode width (pouch cell only)	[m]
		h_e	Electrode height (pouch cell only)	[m]
		$V_{eq\,c}$	Equivalent unit channel volume	[m³]
		$N_{eq\,c}$	Number of equivalent channels	—
		R⟨x⟩	Radial pattern with ⟨x⟩ equivalent channels (coin cell only)	—

(Continued).

Acronym/symbol	Full name	Unit
K⟨x⟩	Clock pattern with ⟨x⟩ equivalent channels (coin cell only)	—
C⟨x⟩	Circular pattern with ⟨x⟩ equivalent channels (coin cell only)	—
B⟨x⟩	Branch pattern with ⟨x⟩ equivalent channels (coin cell only)	—
V⟨x⟩	Vertical pattern with ⟨x⟩ equivalent channels (pouch cell only)	—
GA-C-⟨x⟩	GA-based pattern with ⟨x⟩ equivalent channels (coin cell only)	—
GA-Pa-⟨x⟩	GA-based pattern with ⟨x⟩ equivalent channels (pouch cell only, infiltration from all edges except top one)	—
GA-Pb-⟨x⟩	GA-based pattern with ⟨x⟩ equivalent channels (pouch cell only, bottom infiltration case)	—

Mass deployment of electric vehicles is still hindered by relatively slow lithium-ion battery (LIB) charging rates. The United States Department of Energy (DOE) has identified extreme fast charging as a critical milestone, with a 15 min recharge time target for high energy density cells (>200 Wh kg^{-1}). Among the different strategies to reach this objective,[1] structuring the electrode with channels to provide shorter diffusion paths along the electrode thickness has demonstrated improved rate capability and capacity retention at fast charge.[2–5] A method to determine the optimal shape and spatial distribution of these channels, that together form the so-called Secondary Pore Network (SPN), for a specific application, while accounting for manufacturing technique limitations has not yet been established. An example of a SPN is shown in Fig. 1. The SPN are fully porous domains with dimensions an order higher than the baseline pore sizes in the electrodes. They act as highways to facilitate ionic transport along the electrode thickness.

Controlling the SPN in structured electrodes not only influences the power- and energy-density of cells, but also the cost. The electrolyte wetting process is an expensive step as complete infiltration can takes days, thus requiring expensive storage space and time.[6] Structured electrodes have demonstrated shorter wetting time[7,8] as channels offer highways for both capillary-driven and concentration gradient-driven transport mechanisms. However, the optimal channel pattern for enhanced wetting is also unknown.

In this work, we identify both optimal patterns, for fast charging, and for fast wetting, independently, through use of a genetic algorithm (GA). We acknowledge that different manufacturers might give different weights to performance and cost, which is why we treat these distinctly rather than combined where the balance of performance and cost would be subjective to priorities for a specific case. The final proposed structured electrode is therefore the baseline porous matrix, a Secondary Pore Network (SPN) tailored for fast charging, and separately a Tertiary Pore Network (TPN) tailored for fast wetting, with less than 10% of active material removed in total. The SPN and TPN are not intrinsically different: they are both fully porous domains with dimensions order higher than baseline pore sizes in the electrode. Their distinction lies in their main function or objective (fast charge in the case of the SPN and fast wetting in the case of the TPN). In this work, we will later see that the optimal pattern for each function differs significantly, thus further justifying a different terminology for each network. The choice to investigate independently SPN for electrochemical optimization and TPN for wetting optimization is also further justified in the discussion section. The next section provides a brief overview of structured electrodes and GAs.

Acronyms and symbols are listed in a nomenclature at the end of article.

Review of Structured Electrode Channel Patterns

Structured electrodes can be achieved through various techniques including co-extrusion, laser ablation, mechanical milling, and freeze casting, for which a review is available in previous work.[9] Some processes, such as laser ablation, are compatible with existing roll-to-roll electrode manufacturing process, and thus compatible with high-throughput and minimal additional manufacturing cost.[10,11] Scaled battery electrode laser structuring has been demonstrated for large-format pouch cells (nominal capacity 2.9 Ah) in an industry-oriented pilot line for LIB production to assess its industrial feasibility.[12] Chen et al., also demonstrated this new manufacturing technique for industrially relevant cell format (>2 Ah pouch cells).[13] Direct laser interference patterning[14] and laser in hollow cylinders[15] have been also demonstrated in a roll-to-roll system, respectively, with web speed of 1.3 m min^{-1} with a web width of 150 mm and 2.6 m min^{-1} with a web width of 120 mm. Additionally, laser ablation offers relative fine control of the channel geometry, which is essential to maintain manufacturing uniformity.

The main goals of the present manuscript are to enhance through-plane ionic diffusion and mitigate degradation (lithium plating) for ultrathick electrodes and/or fast charging.[5,16] In the case of laser ablation, there is a trade-off between capacity and power.[17] Within reason, the more material you remove the better the cell's rate capability, but since active material is removed during ablation the battery's capacity will be proportionally lower. Therefore, it is considered suboptimal to remove electrode material up to the current collector interface. Instead, several groups intentionally left a relatively thin layer of unstructured material to conserve active material while still gaining rate[12,17,18] benefit. The as-manufactured electrode is then a dual layer with a power layer (separator side, structured) and an energy layer (current collector side, unstructured).[20] The shape of the as-produced channels is strongly dependent on the structuring technique, with typically a trapezoidal cross-section shape realized in co-extrusion and laser ablated processes.[5] Two patterns have thus-far been reported in the literature: groove lines[2,3,5,17–21] and cylindrical channels,[4,10,18,22–26] each with sub-variants: 1D lines[2,3,17,21] or cross lines (i.e., micro pillars),[20] and square[18,23] or hexagonal[4,10,22,24–27] pattern, respectively. The optimal distribution of such channels is not known.

While channels have been introduced primarily to improve through-plane ionic diffusion, improvements have been also reported on electrolyte wetting.[7,8] Habedank et al.[8] demonstrated a significant wetting time reduction from 40% porous unstructured to 30% porous laser-structured electrodes, under realistic production conditions for

a pouch graphite/nickel manganese cobalt oxide (NMC) cell. Pfleging et al.[7] measured tremendous discharge capacity difference between unstructured and laser-structured NMC if cycled immediately after electrolyte filling and lithium-ion cell assembly, and lower but still significant difference after 24 h storage, where in both cases the structured cell had improved wetting. Modeling work on standard dual layer electrodes indicated that electrolyte infiltration can be facilitated by carefully tuning the microstructure properties of each layer.[28] Berhe et al.,[29] investigated impact of laser-structured groove channels on lithium iron phosphate (LFP) electrode with capillary rise test, wetting balance test and rate performance test, with different channel depths and aspect ratios. The authors show the influence of gravity goes up as the capillary height increases, and that increasing the channel aspect ratio improves wettability. Models capturing the wetting process on the baseline, unstructured, electrodes indicate the presence of residual gas after electrolyte infiltration, which results in degraded effective transport parameters.[30,31] It is believed that introducing channels in the microstructure can reduce the amount of residual gas and thus improve performances.

While other groups have already investigated structured electrodes, and to some extent performed some parameter space analysis on the channel dimensions and/or patterns,[27,32,33] there is not (to the authors knowledge) a channel design identified as optimal from an optimization analysis (that is not form a list of predetermined patterns or a list of dimension parameters, but from the full design space without parameter down selection). For instance, for the SPN, grooves lines and cylindrical channels organized in a regular hexagon pattern are the two cases typically investigated in the literature, even though these two patterns only represent a tiny fraction of the whole design space. Their frequent usage in the literature is motivated by their simplicity and relative ease to manufacture for the groove lines pattern, and from the *implicit* assumption that regular holes are optimal. This is even more relevant for the TPN for which there is not yet a pattern thought to be optimal already identified in the literature to optimize wetting performance. In this regard, the optimization approach developed in this work is first tested to optimize fast-charge performance (the SPN), for which cylindrical holes periodically organized is expected to be optimal. After identifying an optimal pattern for fast-charging, the optimization approach is used to determine the best designs for fast wetting, which has not been yet proposed in the literature. In this work, we propose to identify the optimal top-down view patterns for fast charging and fast wetting, separately, separately, using a specified low material loss constraint. Due to the large design space, as further explained in the *Results* section, it is unrealistic to explore the full design parameter space manually. Instead, an in-house genetic algorithm (GA) is used to identify the optimal patterns. The next section provides an overview of GAs used in the battery field.

Review of genetic algorithm used in battery modeling.—GAs are a class of stochastic algorithms which are well suited for large-scale, constrained and unconstrained, single- and multi-objective, optimization problems. Unlike standard algorithms that iterate on a unique solution according to a deterministic approach, GAs iterate on a population *p* of solutions (where each solution is called an *individual* or a *chromosome*) emulating the concept of biological/ Darwinian evolution with stochastic operators to generate the next population.[34] GAs are relatively simple mathematically and robust in regards to local minima (as long as the initial population starts with high diversity), which explains their success in a wide range of applications.[34] However, GAs can be very CPU-expensive since the objective function (also called *fitness function* in the GA terminology) must be called for each individual of the population, at each iteration. Continually calling the objective function can result in potentially thousands of calculations, which can restrict the GAs application if the fitness function is not carefully selected. Furthermore, a preliminary *encoding* step is required to convert the problem in an input intelligible by the method, which is problem-specific and can be challenging. Lastly, one interesting facet of GA

is that while the concept relies on a simple recipe based on three main stochastic operators (i.e., *selection*, *crossover*, *mutation*, which are further defined in the *Numerical methods* section), there are many variants for each of operator, which provides avenues to finely tune a GA for a particular problem.[34]

GAs have been used to solve a variety of LIB optimization problems in the literature and are summarized below:

• *Model parameter identification.* Parameter identification is a well-suited problem for GAs, as the encoding step is straightforward with parameters encoded as a list of numbers (i.e., value encoding scheme[34]), and macroscale LIB models are typically relatively fast. Zhang et al.[35] identified 27 parameters (both microstructure and material coefficients) of a pseudo 2-dimensional (P2D) model including temperature dependence for two different cell chemistries (graphite/LiFePO$_4$ and mesocarbon-microbeads/LiCoO$_2$). Their multi-objective (4) optimization consisted of reducing prediction errors on both cell voltage and surface temperature for cylindrical batteries, considering two room temperatures (15 °C and 30 °C). As no set of parameters can optimally satisfy all four objectives, a set of nondominated solutions (Pareto front) is first identified instead, using a modified Nondominated Sorting Genetic Algorithm (NSGA-II),[36] and a final selection is then performed using the Technique for Order Preference by Similarity to Ideal Solution (TOPSIS),[37] which is a multiple criteria decision-making method. Accurate fitting was obtained with a population of 400 individuals after 200 generations (i.e., a total of 80,000 P2D simulations), for a calculation time of 19 h per cell with parallelized code running on a cluster. J.C. Forman et al.[38] identified 88 parameters of a P2D model (with open circuit potential (OCP) and conductivity functions being described with dozens of control points) based on a single-objective function (cell voltage). Only part of the cycling data was used for fitting the coefficients, while the remaining part was used to validate the fitting. Parallelization was also used to distribute the calculations on 5 quad core computers to finish the optimization in 3 weeks. GAs were also used for parameter identification of equivalent circuit model.[39–43]

• *State of Health (SOH) and State of Power (SOP) estimations.* Meng et al.[44] estimated the battery SOH from partial charging, with optimal voltage ranges selected using NSGA-II considering a bi-objective optimization problem: maximizing estimation accuracy, while minimizing the length of the voltage range. The authors identified two optimal voltage ranges for SOH estimation, which provides more flexibility as the battery management system can then estimate the SOH at different charging states of the battery. Wang et al.[45] identified SOH through incremental capacity analysis. The peak positions of the incremental capacity curves are extracted as health factors and then correlated with the SOH through a Gaussian Process Regression model, for which the hyper parameters have been calculated either with a baseline conjugate gradient method or with a GA. The authors used a multi-island genetic algorithm that provide an additional operator, *migration* (between islands, i.e., isolated groups of individuals), to keep high diversity and thus reduce the risk of finding a local optimum instead of the global one. Lu et al.[46] compared a baseline Taylor expansion method and a GA-based method for SOP estimation. Unlike the Taylor expansion method, which is plagued with a time-increasing remainder error, the GA has been found suitable for long time-scale estimation with associated improved predictions.

• *Charge profile.* Yan et al.[47] identified an optimal charge profile to minimize charging time and temperature increase. The authors found the Pareto front of the GA-based charge profile dominated the baseline CC–CV charge profile. Liu et al.[48] proposed to optimize both electrode porosity, thickness, and particle size with charge profile parameters to identify the optimal doublet {electrode, pulse charge profile} for a multi-objective problem: minimize temperature rise, charging time, and side-reaction current.

• *EV fleet charge scheduling, infrastructure, and cost analysis.* Milas et al.[49] used GA to optimize the charging time and cost of a fleet of electric vehicles and to deliver personalized solution for each

vehicle based on user-defined criteria, while also maximizing charging station utilization and battery health, considering a non-uniform set of available chargers (normal and fast chargers). The authors use a coupled two-layer chromosome genetic algorithm, with the first layer identifying the charger, and the second layer associated with charging current for a given time slot. Elmehdi et al.[50] used GA to identify the optimal vehicle-to-grid and grid-to-vehicle operations considering various charging and discharging price periods. Celli et al.[51] used NSGA-II for planning integrated power distribution and charging stations on a coupled traffic network and distribution network derived from a real world study to minimize the investment cost and the average waiting time for charging.

To our knowledge, it is the first time GA is used to identify optimal channel patterns for fast charging and fast wetting.

Aim and organization of the article.—This article is focused on identifying the optimal patterns for the SPN and the TPN for fast charging and fast wetting, respectively. Ideally, a 3D electrochemical model and a 3D fluid dynamics model would be used for such tasks. However, these models are CPU-expensive and thus not suitable for a GA-based optimization approach that requires evaluating the model thousands of times. Instead, two CPU-cheap 2D distance-based fitness functions (one for the SPN and one for the TPN) are assumed to be monolithically correlated with the electrochemical performances or the wetting, as further explained in the section *Numerical methods*, are used to identify the optimal patterns of the SPN and the TPN. The model presented in this work is then not physics-based but distance-based to make it fast enough for the GA approach. Predicted improvements are thus not expressed in typical battery metrics (e.g., capacity, wetting coverage) but in distance-based metrics assumed to be monolithically correlated with the former (even though the correlation itself is unknown). This approach allows us to identify the optimal patterns (due to the *monolithic* correlation between the two metrics), albeit without quantifying the electrochemical or wetting improvement using typical battery metrics (due to the *unknown* correlation between the two metrics). In other words, the model is focused mainly on identifying the optimal patterns, rather than on quantifying the improvements provided by them (physics-based models are more suited for this second task). While the method itself is adimensional, physical length is introduced knowing cell and channel dimensions to provide practical design recommendations. The present work identifies the pattern's overall shape to narrow down the associated parameter space, enabling physics-based 3D models to later refine the design recommendations using a smaller design space in future work. Furthermore, the complex patterns identified with the GA-optimization approach are compared with simpler, easier to manufacture, patterns to estimate if extra complexity adds significant or only incremental benefits.

The article is organized as follows. Section *Laser system, electrode, and channel dimensions* provides shape and dimensions of channels obtained with our experimental laser system, which are required to dimensionalize the problem and restrict the optimization problem within the realm of manufacturing capabilities. Section *Simpler patterns and comparison methodology* introduces simpler patterns selected for the comparison with the optimal patterns identified using the GA. Section *Numerical methods* defines the optimization problem and details the genetic algorithm as well as the choice of the distance-based fitness functions and how to interpret the results. Section *Results* provides the optimal channel distribution for both SPN and TPN with some additional analysis specific to each pore network. For fast charging (SPN), a permutation analysis (i.e., brute force approach, that is testing all possible solutions of the parameter space) is performed on a small grid to validate the GA prediction. The optimal distribution is also compared with a random channel location and with a baseline groove lines pattern. For fast

wetting (TPN), two cell form factors are considered: coin cell and pouch cell. Optimal distributions are compared with simpler, easier to manufacture, patterns specific to each form factor. The *Discussion* and *Conclusions* sections provide insight and recommendations for adopting electrode microstructure patterns.

Laser System, Electrode, and Channel Dimensions

The pre-calendared electrodes were patterned with a bench-top diode-pumped solid-state femtosecond laser (Advanced Optowave FEMTO-IR-1030) with a 1030 nm emission wavelength (λ) and $\approx$ 600 fs laser pulses with tunable repetition rates between 100 kHz–1 MHz and average power of $\leqslant$11 W at 100 kHz. A high-speed scanning system with galvanometer-controlled mirrors (Aerotech, Inc., AVG10HPO) and an f-theta-Ronar telecentric lens (LINOS, λ= 1030−1080 nm) with a focal length of 70 mm was used to direct and focus the laser beam to a $\approx$25 μm spot size. The laser spot size was estimated using a silicon substrate as direct observation through a camera is not possible (the laser would have burn the detector).[52] Electrode laser ablation was achieved with pulse energies of approximately 15 μJ pulse^{-1} or 3 J cm^{-2} fluence. Electrode ablation was carried out in ambient air under a directed flow of nitrogen gas that pushed ablated debris into a vacuum exhaust tube positioned close to the electrode surface to remove ablated materials, preventing their re-deposition. The $\approx$25 μm spot size ablates channels with a minimum of around 40–50 μm diameter cylindrical channel or groove width[5] (cf, Fig. 1). The width of the channel is influenced by how deep the ablation goes due to the ablation area having a slope from top to bottom of the channel. Cross section imaging[5] indicates a channel slope θ_c of roughly 75°. Cross-section imaging indicates some shape and size variations from channel to channel, especially in the hole configuration (cf, Fig. 1c) and will be the subject of a future article.

Analysis is performed on commercial electrodes provided by Clarios, with specifications listed in Table I. Extension to other electrode materials is later discussed in the *Model range of validity and results interpretation* section.

Specifics for SPN (fast charging).—Grooved channels will serve as baseline comparison, while the optimal location for the disc-like laser ablation pattern is determined using the GA. The disc-channel volume is calculated according to Eq. 1a, with t_c^{max} the maximum thickness of the channel for a given channel slope θ and channel top width w_c^t, V_c^{max} the maximum channel volume with the associated maximum channel thickness, t_c the actual thickness of the channel, t_e the electrode thickness, w_c^b the channel bottom width, V_c^b the volume of the bottom channel, and V_c the actual channel volume (subtraction of full cone and bottom cone volume). In the case that the channel extremities meet at its bottom tip (that is channel bottom width w_c^b = 0, cf, Fig. 1d), then the volume of the bottom channel V_c^b would be 0. These variables are also labelled in Fig. 1d. Electrode volume within the field of view (FOV) $V_{e,FOV}$ is calculated according to Eq. 1b, with g_r and g_c the FOV number of pixels (row and column, respectively) and s the pixel size. In our model, the FOV is the 2D region of space modeled discretized in g_r times g_c pixels with each pixel being an element of surface (either porous baseline electrode or channel) of size s^2. As discussed later in *Problem definition and optimization function*, periodic boundary conditions are used so that the full electrode volume does not need to be represented. The total channel volume in the FOV $V_{c,\,tot}$, and the number of channels in the FOV N_c is then deduced according to Eq. 1c. For N_c the closest integer from the numerical value is selected (cf, Eq. 1c, "round"). The laser system enforces $\theta_c = 75°$ and $w_c^t = 50\,\mu$m. The channel width w_c^t for SPN is selected as the minimum diameter the laser system can provide for disc-shaped channels, as large channels are not required to provide ionic transport enhancement (at the condition they are still larger than

the porous matrix pores). Furthermore, too large of channels can lead to unnecessary material loss resulting in suboptimal performance.[23] Analysis is performed on the cathode side, with electrode thickness of $t_e = 67\ \mu m$ and channel thickness ratio r_t of 0.5. The grid FOV is $g_r = g_c = 120$, and pixel resolution $s = 5.56\ \mu m$ (such that the disc diameter has a 9-pixel length). The channel volume ratio r_V is set to 5%, which is equivalent to 33 channels in the FOV. For electrode without macroscale heterogeneity (no gradation along thickness), this would correspond to a 5% active material mass loss.

$$t_c^{max} = \frac{w_c^t}{2}\tan(\theta_c)\quad V_c^{max} = \frac{1}{3}\pi\left(\frac{w_c^t}{2}\right)^2 t_c^{max}\quad t_c = r_t t_e,\ r_t \in [0,1]$$

$$w_c^b = \frac{2(t_c^{max} - t_c)}{\tan(\theta_c)}\quad V_c^b = \frac{1}{3}\pi\left(\frac{w_c^b}{2}\right)^2(t_c^{max} - t_c)\quad V_c = V_c^{max} - V_c^b \qquad [1a]$$

$$V_{e,FOV} = t_e g_r g_c s^2 \qquad [1b]$$

$$V_{c,tot} = r_V V_{e,FOV}\quad N_c = \text{round}\left(\frac{V_{c,tot}}{V_c}\right) \qquad [1c]$$

Specifics for TPN (fast wetting).—Channels consist of arbitrary lines with a trapezoidal cross section of area A'. For the coin-cell form factor, we determine an equivalent unit channel volume $V_{eq\,c}'$ corresponding to the volume of a channel radially oriented (i.e., along the diameter d of the coin cell). This allows us to later translate an arbitrary pattern in an equivalent number $N_{eq\,c}'$ of radially oriented channels, which is useful for comparison with other patterns (cf, Eqs. 2a, 2b and 2c). For $N_{eq\,c}'$ the closest integer from the numerical value is selected (cf, Eq. 2c, "round"). The notation is identical to the fast-charging case (SPN), except for the apostrophe' to identify the coin cell case when required. The laser system enforces $\theta_c' = 75°$ and $w_c^{t'} = 40\ \mu m$. The channel width $w_c^{t'}$ is not a recommendation as further explained for the pouch cell case. Here, we choose to select the minimal size provided by the laser system for a line-based pattern. The electrode thickness $t_e' = 75\ \mu m$ and diameter $d = 15\ mm$, channel thickness is half of the electrode thickness $r_t' = 0.5$. The whole coin cell geometry is represented as later explained in the "*Problem definition and optimization function*" section. Different r_V', and thus $N_{eq\,c}'$, are investigated, from 0.5 to 2% and from 4 to 16, respectively for r_V' and $N_{eq\,c}'$. The total material volume loss for a combined SPN and TPN ranges from 5.5 to 7% for the coin-cell case. To match the pixel length with the real channel width, 375 pixels along the diameter are needed. Such resolution is too CPU-expensive (not only the calculation for each

individual is higher, but the population size needs to be increased to achieve convergence as the number of permutations, that is the parameter space, is increasing). To remedy this issue, the algorithm is run several times using a number of pixels along the cell diameter from 81 to 201 (that is a grid or mesh resolution sensitivity analysis) to check the pattern shape and associated fitness convergence.

$$V_{eq\,c}' = dA'\quad A' = t_c'\left(w_c^{t'} - \frac{t_c'}{\tan(\theta_c')}\right)\quad t_c' = r_t' t_e',\ r_t' \in [0,1] \quad [2a]$$

$$V_e' = \pi\left(\frac{d}{2}\right)^2 t_e' \qquad [2b]$$

$$V_{c,tot}' = r_V' V_e'\quad N_{eq\,c}' = \text{round}\left(\frac{V_{c,tot}'}{V_{eq\,c}'}\right) \qquad [2c]$$

For the pouch-cell form factor, we determine an equivalent unit channel volume $V_{eq\,c}''$ corresponding to the volume of a vertically oriented channel (cf, Eq. 3a and Fig. 2 right). This choice is motivated by the electrolyte wetting process for which electrolyte is dropped from the top and then infiltrates the porous matrix from the bottom through capillarity forces.[53] The electrode volume is provided with Eq. 3b, with w_e and h_e, respectively, the width and the height of the electrode. Number of equivalent channels $N_{eq\,c}''$ is deduced using Eq. 3c. Notation is identical with previous cases, except for the double apostrophe '' to identify the pouch cell case, when required. The electrode (arbitrary) dimensions are $t_e'' = 75\ \mu m$, $w_e = 50\ mm$, and $h_e = 75\ mm$. Channel dimensions are $\theta_c'' = 75°$, $w_c^{t''} = 80\ \mu m$, $r_t'' = 0.5$. A larger channel width is selected to keep grid size low enough to allow a reasonable calculation time. It is expected however that the optimal channel width for TPN would be maximum at the electrolyte entry-edges, and then the channel width would decrease as the channel permeates to the center of the electrode sheet due to fluid dynamics consideration.[54–56] To determine a channel width that considers fluid-dynamics, a physics-based model is required, which is outside the scope of this work. Considering fluid-dynamic effects, it is then possible that channel maximum width for TPN would exceed the minimum width provided by laser system, especially for large format cells. This remark applies also for the TPN coin cell. Thus, the channel width selected in this work for both coin cell and pouch cell TPNs are then not recommendations, but a choice resulting from computational time constraint and laser system capabilities (unlike for SPN for which channel width used *is* the recommendation). The whole pouch-cell geometry is represented. Different r_V'', and thus $N_{eq\,c}''$, are investigated, from 0.5 to 1.5% and ≈ 7 to ≈ 21, respectively for

Table I. Electrode, cell specifications, and associated model parameters before laser ablation. Negative to positive capacity ratio (calculated from the other parameters listed in the table), is required to determine the active material volume to ablate in each electrode to reach a given ratio after laser ablation.

|	Anode	Cathode
Active material	Graphite	$LiNi_{1/3}Mn_{1/3}Co_{1/3}O_2$
Model parameter: Thickness (μm)	75	67
Weight loading, active material/conductive carbon/binder (%)	96/1/3	95/3/2
Density, active material/conductive carbon/binder (g.cm^{-3})	2.2/1.9/1.8	4.69/1.9/1.8
Volume fractions (pore/active material/additives)	0.37/0.6/0.03	0.32/0.6/0.08
Areal capacity (mAh.cm^{-2})	3.22	3.081
Coin cell disk diameter (mm)	15	14
Maximum Li concentration in active material, $C_{s,max}$ (mol.m^{-3})	28000	49000
State of charge range of x in Li_xC_6 and $Li_xNi_{1/3}Mn_{1/3}Co_{1/3}O_2$	[0–1]	[0.3–0.91]
Capacity for $1 \times 1\ \mu m^2$ of electrode, C_b (C)	1.2155e^5	1.1600e^5
Model parameter: Baseline negative to positive capacity ratio, N/P_b	1.0478	
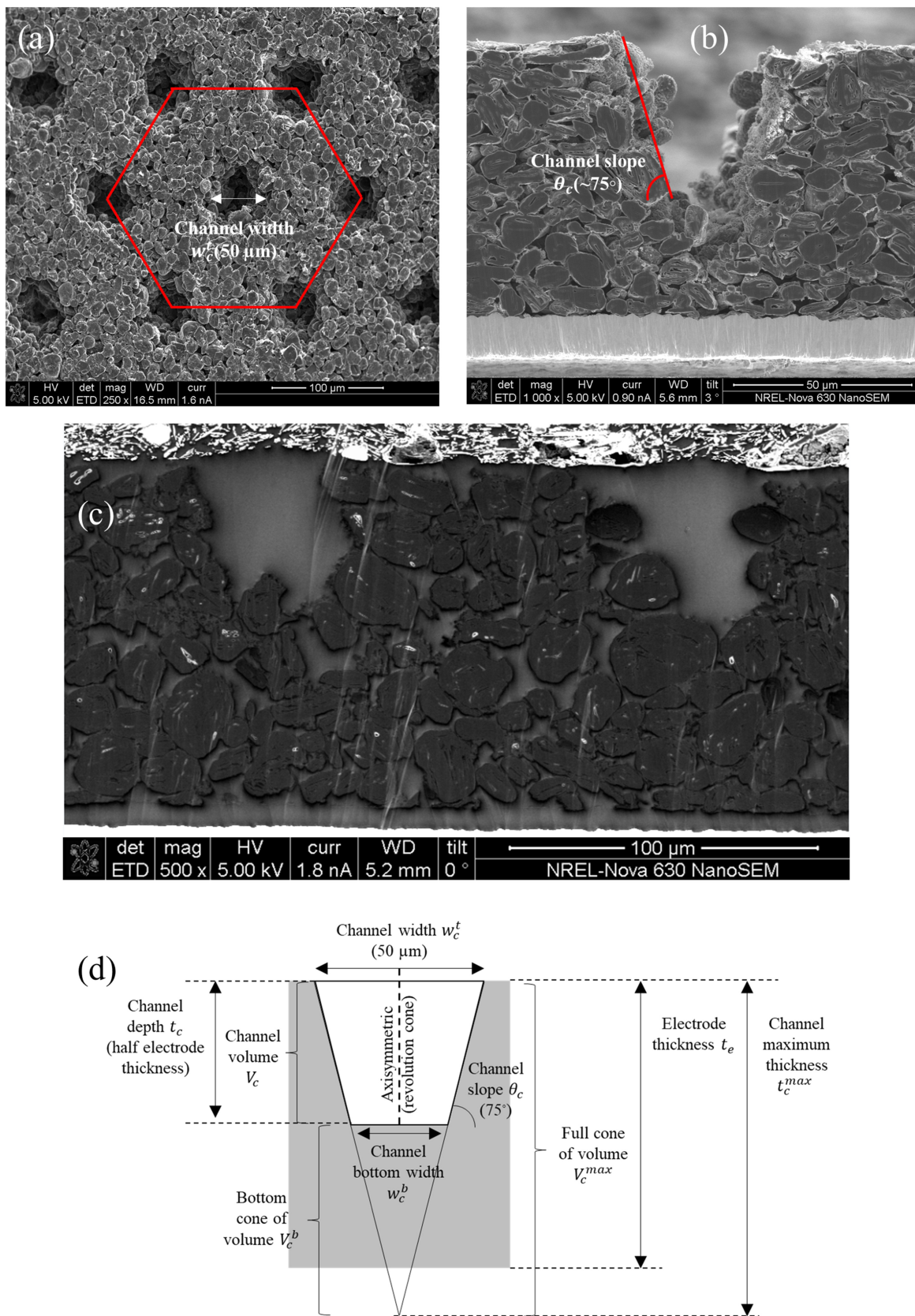
Figure 1. Scanning electron microscopy (SEM) images of a structured graphite electrode prepared with NREL laser system, illustrated for (a) top-down perspective with holes (b) cross-section perspective with grooved lines, and (c) cross-section perspective with holes. (d) Idealized channel dimension used to set up the grid problem.

$r_V{''}$ and $N_{eq\,c}{''}$. The total material volume loss for a combined SPN and TPN ranges from 5.5 to 6.5% for the pouch-cell case.

$$V_{eq\,c}{''} = h_e A{''} \quad A{''} = t_c{''}\left(w_c^{t{''}} - \frac{t_c{''}}{\tan(\theta_c{''})}\right) t_c{''} = r_t{''} t_e{''}, \; r_t{''} \in [0, 1] \quad [3a]$$

$$V_e{''} = w_e h_e t_e{''} \quad [3b]$$

$$V_{c,tot}{''} = r_V{''} V_e{''} \quad N_{eq\,c}{''} = \text{round}\left(\frac{V_{c,\,tot}{''}}{V_{eq\,c}{''}}\right) \quad [3c]$$

Simpler Patterns and Comparison Methodology

The comparison for SPN is straightforward as pixels represent channel area in a 1:1 ratio. The number of pixels (i.e., sum of channel area) is then used to compare different patterns. Patterns that provide lower fitness function, as defined later in the *Numerical methods* section, for the same total channel area are considered better. The optimal pattern is compared with grooved lines, i.e., straight lines vertically, or horizontally (but not both) aligned with same width, and with disc channels randomly distributed (cf, Fig. 2). Grooved lines require a less complex laser system setup because the beam can simply be split into parallel beams on the electrode roll travelling in the web direction. Cylindrical channels require more complex optics controls such as a polygon system to spatially distribute the pulses. Last, the randomly distributed disc channels case is used as an extreme case to evaluate the negative impact of poor manufacturing control on the channel locations.

The comparison for TPN is more complicated than the SPN, as the pixel area overestimates the actual channel area. The mismatch between pixel size and channel width implies the apparent channel surface coverage is higher than the one that is actually modeled, especially for the low grid resolution. Because the complex shape of the as-generated channel patterns and the size mismatch mentioned above, the pixel representation is inadequate to represent the real length of the channels, as one pixel can contain different channels. Furthermore, the pixel representation does not discriminate between vertical or horizontal path. This lack of direction fidelity results in different channel lengths. For example, the true length is 1 pixel length for the vertical path, while the diagonal path has a true length of $\sqrt{2}$ pixel length. To remedy this issue, an in-house tree-branching algorithm identification is used to identify the effective length of the channels (cf, Fig. 3). This algorithm is simply based on if-else statements that recognize the different possible channels junctions and then assign accordingly a length per pixel. This is particularly important to compare with some baseline predetermined channel patterns (e.g., radially, or vertically oriented channels), for which the true length is known. Furthermore, the laser system requires the exact line geometry to structure the electrodes and is provided by this algorithm identification.

Optimal TPN patterns are compared with several simpler patterns (cf, Fig. 2) using both apparent surface coverage and effective length. Note that comparison is performed with both optimized and predetermined patterns at the same grid resolution (and not with the ideal, infinite resolution, of Fig. 2). Radial and vertical patterns are the most obvious choices because the electrolyte typically infiltrates from perimeter to center during vacuum filling procedures. However, the radial pattern appears suboptimal as channel density is likely unnecessarily high near the electrode center. The clock pattern is a tentative design to remedy the increased channel density issue at the center. Additionally, several authors report an effective way to optimize a cooling network within a domain is achieved with a tree-shaped (or branching) network.[55–57] The circle and branch patterns attempt to capture these tree-like patterns. These predetermined patterns have been manually selected to provide comparison points based on educated guesses as mentioned above (channel
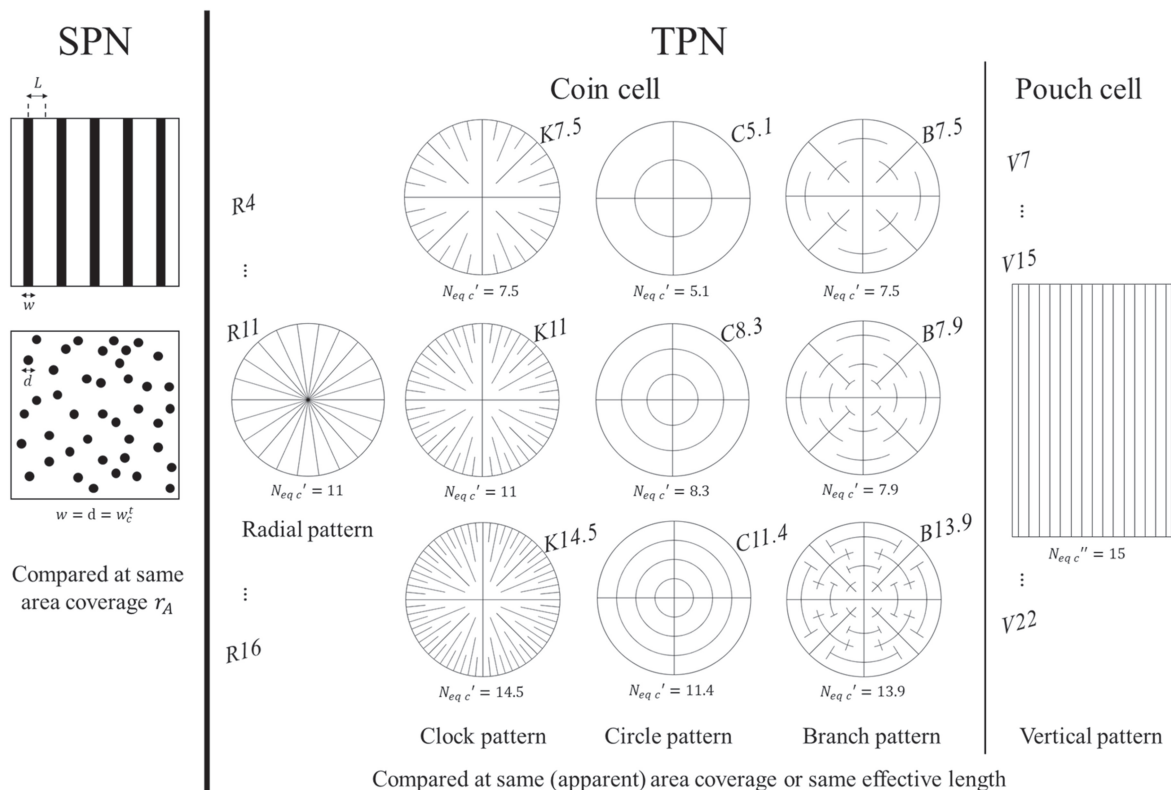

Figure 2. SPN and TPN patterns to be compared with patterns identified with the GA-optimization approach. Labels (e.g., R11) indicate pattern type (R: radial, K: clock, C: circle, B: branch, V: vertical) and equivalent channel number (number of diameter and vertical lines, respectively for coin and pouch cell) and will be used in subsequent graphs to identify patterns. Labels are used in Figs. 11–14 (with GA-* referring to patterns obtained with the GA optimization approach).

should transport electrolyte from edges to center and literature indicates branching is relevant). Pattern periodicity is assumed even though periodic length, if any, is unknown.

Numerical Methods

Problem definition and optimization function.—As stated in the introduction, using a physics-based model is not compatible with the GA-based approach proposed in this work. Instead, we define a CPU-cheap fitness function, which is to be negatively correlated with the cell overall performance enhancement induced by the SPN channels, and a second fitness function that is assumed to be negatively correlated with the wetting time reduction induced by the TPN channels. In both cases, a constraint is set on the electrode material total loss induced by creating channels, with an additional connectivity constraint for the TPN case.

Fast charging.—The electrode material near the SPN channels is expected to become more electrochemically active as compared to an unstructured electrode case, because the SPN introduces facile pathways for Li-ion migration and diffusion. If electrode active material is located below the channels (i.e., close to the current collector) in a dual-layer setup, the remaining ionic diffusion distance in the tortuous porous matrix is the electrode thickness minus the channel thickness. If electrode material is located between channels, the relevant diffusion distance is the minimum between the distance from the separator and the distance from the nearest channel, neglecting diffusion anisotropy. In the latter case, for electrode volumes near the current collector and far from channels, the positive impact of the channel introduction is reduced. If electrode material is far enough away from the SPN channels, the electrode material will behave independently (in-plane wise) from the rest of the electrode and may consequently suffer from ionic transport limitations. Therefore, an obvious solution is to distribute the channels to minimize the in-plane distance between the porous matrix and channels.

The fitness function for a given channel distribution is then the average of the Euclidean distance map (EDM), defined as the minimal distance from the porous matrix to any channel, cf, Eqs. 4a and 5. This definition is adequate for rectangular groove lines, but less effective for cylindrical channels. Indeed, if cylindrical channels are optimal, the current definition will assign 1 pixel per channel, resulting in an extremely poor grid resolution and neglecting the impact of the rounded shape of the channel. To prevent this, a second definition with a shape constraint, discs of radius r, is introduced (cf, Eq. 4b). Last, to limit edge effects and

reduce the required field of view (FOV), periodic boundary conditions are used, as illustrated in Fig. 4a with discs. The EDM is calculated with the MATLAB built-in function *bwdist*, with additional coding to implement the periodic boundary condition. The number of points N in Eqs. 4a, 4b is the number of channels N_c. The number of pixel p assigned to the channel domain is equal to N in Eq. 4a but is larger than N in Eq. 4b with p equal N times number of pixel per disc.

> Given a 2D array I with $I(i, j) = 0$ (porous matrix)
> and an integer $N > 1$, find optimal location
> of N points for which $I(i_k, j_k)$
> $= 1, \forall\ k \in [1, N]$, *i.e.*, $sum(I)$
> $= N$ that minimize the average
> Euclidean distance map EDM   [4a]

> Given a 2D *array* I with $I(i, j) = 0$ (porous matrix)
> and an integer $N > 1$ and a radius $r = w_c^t/2$,
> find optimal location of N points for which
> $I(i_k, j_k) = 1, \forall\ k \in [1, N]$ and $I(\text{EDM}(x) < r) = 1$
> that minimize the average Euclidean distance map EDM   [4b]

$$\text{with EDM}(x) = \min\{\text{dist}(x, y)\},\ \forall\ x \text{ with } I(x)$$
$$= 0 \text{ and }\ \forall\ y \text{ with } I(y) = 1 \tag{5}$$

Analytical fitness for groove lines is calculated according to Eq. 6 (average distance between two points is half the distance between them). Apparent channel coverage r_A is set equal to that obtained with the disc channel. Periodic length L is noted in Fig. 2.

$$f_{\text{th, groove}} = \frac{L}{2}(1 - r_A)$$

$$\text{with} \begin{cases} w_c^t/2 = r_A L \text{ and } f_{\text{th, groove}} = \dfrac{L - w_c^t/2}{2} \\ L \text{ groove lines periodic pattern length} \\ r_A \text{ apparent channel coverage} \end{cases} \tag{6}$$

Fast wetting.—In the fast-wetting optimization (TPN), two electrode sheet form factors are considered: a coin-cell, for which electrolyte infiltration occurs at the cell perimeter edge (cf, Fig. 4b, and a pouch-cell, for which electrolyte infiltration occurs from the
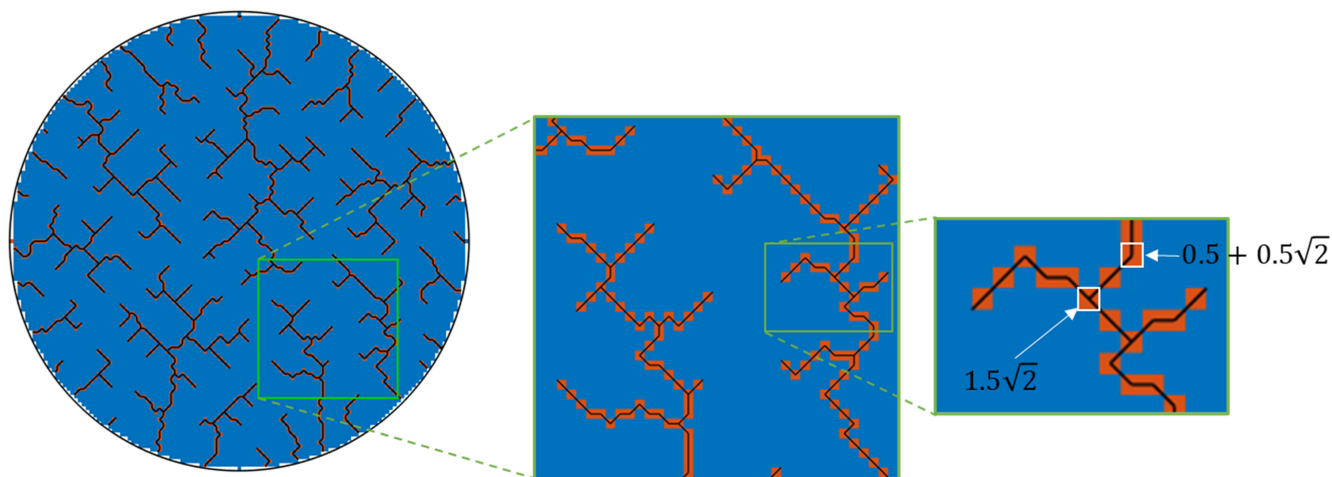

Figure 3. TPN (fast wetting from perimeter) for a coin-cell. Blue and red pixels represent, respectively, the porous matrix and the channels. Solid black lines represent the true channel length and shape. Channel lengths are expressed in pixel length in the illustration but normalized with cell diameter (or cell height for pouch cell) in subsequent TPN results.

bottom side (cf, Fig. 4c) or from all sides except the top one (cf, Fig. 4d). Pouch cell filling typically involves depositing electrolyte from the top of a vertically standing cell, with liquid progressively infiltrating though capillarity from the bottom, and the edges as the filling progress.[53] Compared with the fast-charging case, a connectivity, or percolation, constraint is added: only channels that percolate to the electrolyte entry-edges are considered for the evaluation of the Euclidean distance map. A connectivity check is only evaluated within the fitness function to modify the 2D array I used to calculate the distance map (cf, Eq. 7). That is, no additional parameter is introduced that would otherwise require weighting connectivity and distance separately or use a Pareto Front in an explicit multi-objective scheme.

While we pursue two objectives (maximize connectivity, minimize distance), the connectivity-induced modification of the 2D array I strongly penalizes the distance-based fitness function and thus a second fitness function is not required (cf, Figs. 4b–4d: unconnected channels do not contribute to the distance reduction). In the *Results* section, we will see these objectives and connectivity constraints proved to be an effective strategy as GA eventually eliminates all non-connected channels without the need to explicitly enforce it. Connectivity is performed with the MATLAB built-in function *bwlabel* with face-to-face and node-to-node connectivity. Note that node-to-node connectivity is relevant as we identify the effective, pixel-free, length from the non-ideal pixel representation (cf, Fig. 3). Because of the connectivity constraint, the only relevant pattern is connected lines with one-pixel width, therefore no shape constraint is added unlike for the fast-charge (SPN) case. Therefore, Eq. 4a (and 7) is used to calculate the EDM, with number of points N equals to the number of pixel p assigned to the channel domain.

No symmetric or periodic boundary conditions are used in the TPN study for two reasons. First, the periodic length is unknown (the repeating pattern could be contained in a quarter of disc, or one eighth, etc.), and setting a periodic length incorrectly could bias the results. That is, adding a symmetry or periodic constraint would exclude some solutions, among which may include the optimal design. Second, since there is no preferential direction for the coin cell form factor, and no horizontal preferential direction for the pouch cell form factor, the optimal solution should reflect this isotropy. As GAs are stochastic-driven, a low population and/or low diversity could lead toward irrelevant macro-scale differences between regions. Achieving patterns without irrelevant preferential channel directions would then be an indirect indication that the population size is large enough.

$$\forall\, k \in [1, N],\ \text{if } I(i_k, j_k) = 1 \text{ and } \nexists\, a \text{ path from}$$
$$I(i_k, j_k) \text{ to electrolyte entry} - \text{edges, then } I(i_k, j_k) = 0 \qquad [7]$$

Model range of validity and results interpretation.—The model presented in this work is not physics-based but distance-based, due to the necessity of using a CPU-cheap fitness function to be able to use in a GA approach. Therefore, the model does not provide improvements expressed in standard electrochemical metrics (e.g., capacity, wetting coverage) but in distance-based metrics, which are assumed to be monolithically negatively correlated with fast charging and fast wetting performances as explained in previous paragraph. That is, while the function correlating the electrochemical metrics and the distance-based metrics is unknown, the pattern maximizing the first and minimizing the second is the same. Such correlation is likely to be nonlinear as characteristic diffusion time t is a quadratic function of the characteristic diffusion distance L ($t = L^2/D$, with D the diffusion coefficient in the considered diffusion direction) and that ionic transport is only one of several mechanism involved in batteries. Nonetheless, this approach enables us to identify the optimal pattern (which is the focus of this work), albeit without quantifying the associated electrochemical improvements, with the latter requiring a physics-based model to be determined. For examples of experimentally-determined and/or model-predicted electrochemical performances improvements, readers are invited to look at the literature (see *review of structured electrode channel patterns* section) and our previous work.[5]

The model does not consider material anisotropy even though it is a key parameter to model transport limitation in batteries. However, most battery electrode materials exhibit transversal anisotropy with in-plane directions having similar diffusion properties while the through-plane direction along the thickness has a
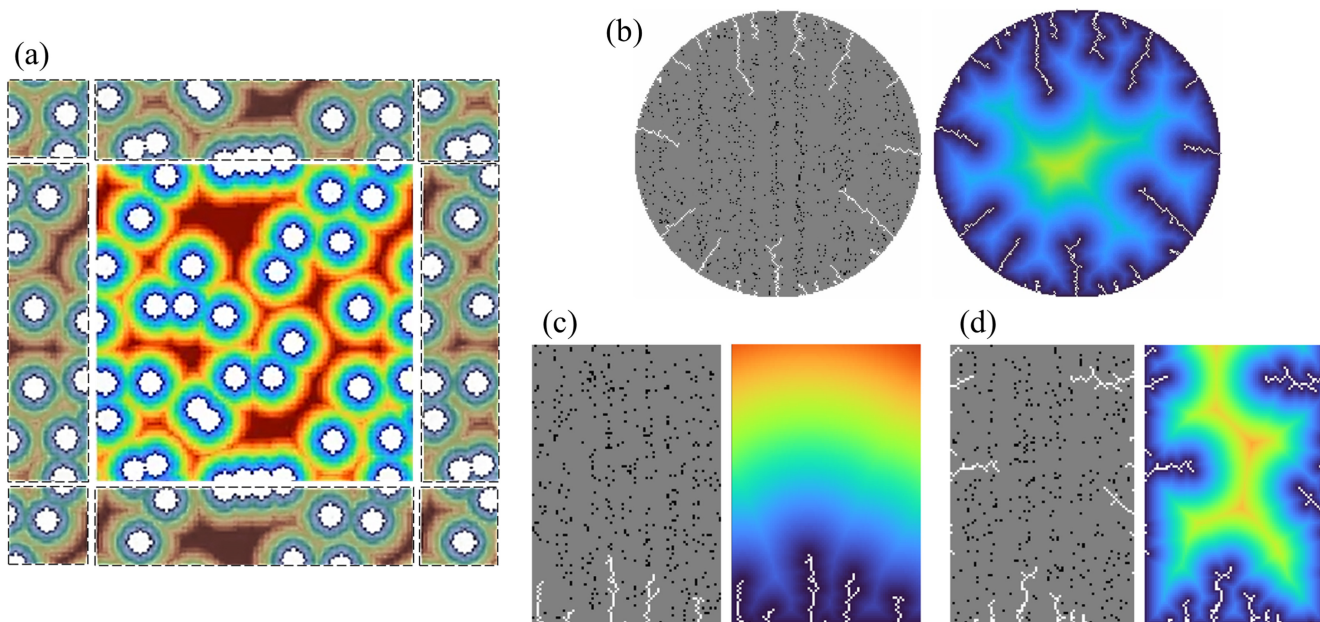

Figure 4. (a) Periodic Euclidean Distance Map *pEDM* illustrated for a distribution of discs for fast charging (SPN). Colormap indicates distance from porous matrix to channel (a: red = 55 μm, b: red = cell radius 15 mm, c and d: red = cell height 75 mm). Centered region represents the FOV, while grey-out out-centered regions are used to enforce the periodicity. (b, c, d) Connected channels (white), unconnected channels (black), electrode material (grey), and associated EDM for fast wetting (TPN). (b) Coin cell, (c) pouch cell with electrolyte infiltration from bottom, and (d) from all edges except the top one. Examples correspond to non-optimal solutions.
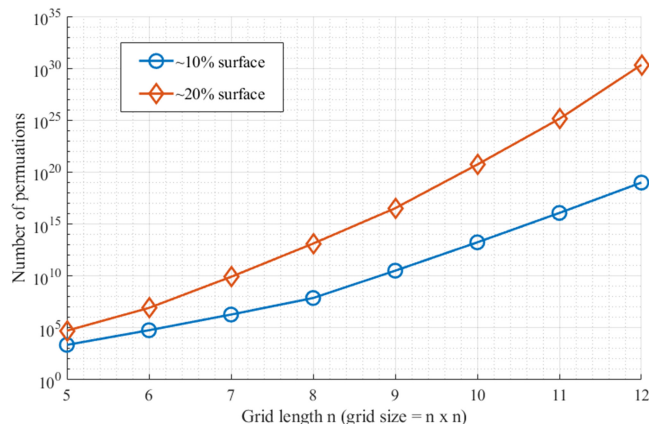
Figure 5. Number of permutations (possible channel spatial distribution in a top-down perspective) for a small grid considering a channel surface coverage of 10 and 20%. Y-axis uses a logarithmic scale. Legend uses "∼" as most data points have a non-integer $r \times N$ that is rounded to use the permutation formula.

poorer diffusion due to particle morphology and calendering.[58] This is especially true for misaligned elongated natural graphite, while other materials such as NMC are roughly isotropic due to the particle near spherical geometry.[59] In this work the isotropy assumption is applied on the two in-plane directions and is thus applicable to a large variety of battery electrode materials. That is, with or without transversal anisotropy the optimal pattern, *that is the focus of this work*, is still the same. In other words, the model range of validity is isotropy or transversal anisotropy for ionic transport in the electrolyte. However, the unknown correlation between the electrochemical performance metrics and the distance-based fitness function, *that is not the focus of this work*, will be different depending on the material anisotropy. For instance, it is expected that misaligned graphite would benefit more, relatively, from the introduction of SPN channels as compared to more isotropic materials at equivalent channel volume, as long as 1) their baseline through-plane Bruggeman exponent p is higher than their in-plane Bruggeman exponent and 2) the baseline in-plane Bruggeman exponent is better for misaligned graphite. Indeed, the introduction of a $p = 1$ pore volume (which is the case in the channels) is more impactful for a baseline high p material, and higher in-plane diffusivity implies channels can be placed further from each other, thus reducing the material loss for equivalent performance improvements.

The model is porosity and material-agnostic (at the condition the range of validity discussed in the previous paragraph is met). That is, optimal patterns are the same for electrodes with different porosities and/or different materials for the same channel volume and thickness, but the previously mentioned correlation between the electrochemical performance metrics and the distance-based fitness function will be different. Last, the model does not consider interaction between electrodes (i.e., the anode/cathode pairing).

Permutation approach.—Considering an n x n grid representing the electrode material from a top-down perspective, we can calculate the number of possible channel patterns for a given number of pixels k assigned to the channels using the permutation formula (cf, Eq. 8). Two cases are considered and plotted in Fig. 5: a surface coverage of 10% ($r = 0.1$) and 20% ($r = 0.2$), the latter being more representative of the real problem as it corresponds to a total material loss of 10% with channel thickness being half the electrode thickness. Even for the tiny grids considered in this example, the number of permutations made it impossible to numerically investigate all of them, even if symmetries was considered. The GA described below remedies this issue. The permutation approach will however be used on small grids to validate the GA and analyze the solution distribution. Furthermore, the permutation approach will

discriminate between grooved lines and cylindrical channels, thus allowing us to choose between fitness function defined with Eqs. 4a or 4b to avoid unnecessary calculations with the less relevant one (grooved lines or cylindrical channels).

$$\frac{N!}{k!(N-k)!} \quad \text{with} \quad \begin{array}{l} N = n \times n \\ k = round\,(r \times N) \end{array} \qquad [8]$$

Genetic algorithm approach.—The GA used in this work has the same approach for both the SPN and TPN. The difference lies in the fitness function itself as detailed in the "*Problem definition and optimization function*" section. The algorithm has been coded in MATLAB from scratch, *without* a dedicated toolbox. Algorithm follows the standard GA approach[34] with the following steps, also illustrated in Table II:

1. *Encoding and initial population.* Equations 1–3 are used to determine the number of channels, and then the number of pixel p to be assigned to the channel domain for each individual. Each individual is encoded in two states: (i) an image-based representation, i.e., a 2D array I the size of the modeled electrode with $I(x, y) = 1$ if pixel belongs to a channel, and 0 otherwise (i.e., binary encoding[21]), and (ii) an indexed-based representation, i.e., a 1D array I' of length p the number of pixels assigned to the channel domain with $I'(k)$ the linear index of pixel k in I, that is $I(I'(k)) = 1 \ \forall \ k \in [1, p]$ (i.e., permutation encoding[34]). The first representation is used for fitness calculation and solution visualization, while the second represents the individual's chromosome used for crossover and mutation operations as further explained. Note that for SPN (disc channel), I' contains only the index of disc centers. For the initial population, individuals are generated with random channel location. Population size $POPs$ is user-defined, and, in practice, is chosen high enough to achieve convergence and reach global minimum. Indeed, a large population size ensures high diversity among the individuals, thus reducing the risk of being trapped in a local minimum.
2. *Compute initial fitness.* The fitness function is calculated for each individual according to Eqs. 4–6. For the TPN, the fitness is normalized with the fitness function for an electrode without channels.
3. *Loop under fitness convergence.*

   a. *Parent selection.* The number of parents P used to generate the next population is equal to the population size times a user-defined ratio, or selection threshold S_p. Individuals are sorted based on their fitness, and the P better are selected to be parents (i.e., truncation selection[60]).
   b. *Crossover.* The number of couples C is half the number of parents. The parents A list is a random selection (without duplicates) from 1 to P of size C. The parents B list is the remaining parents. The algorithm then loops on each couple c\{Parent A_c, Parent B_c\}, and for each couple loops on the number of crossovers C_r per couple, with $C_r = 1/S_p$. Each crossover produces two new individuals for the next generation, so that $2CC_r$ is the initial population size (i.e., the population size is constant over generations). For each crossover, a random crossover point is selected to cut the chromosome I' of each parent (i.e., I_{A_c}' and I_{B_c}') and genetic information of the two parents is swapped to generate two new individuals as illustrated in Table II (i.e., single point crossover[34]). Indices shared between parents are transferred to the two new individuals and removed from the parents' chromosome prior chromosome swapping to prevent duplication. Last, if both parents are identical, a rare statistical event, one child is randomly generated while the second child inherits parent's chromosome as its own.

Table II. Genetic algorithm steps.

Steps	Method	Parameters
1 Generate initial population and encoding	Random distribution. Binary and permutation encoding.	SPN: $POP_s = 1e^3 - 1e^5$ TPN: $POP_s = 5e^3 - 5e^4$
2 Compute initial fitness	Distance-based (with connectivity constraint for TPN), EDM average.	
3 Loop until convergence		Stop if 20 last iterations have fitness min-max difference less than 5e-5.
3a Parent selection	Truncation selection	$S_p = 1/4$ $P = POP_s \times S_p$
3b Crossover	 One-point crossover	$C = P/2$ $C_r = 1/S_p$ $2CC_r = POP_s$
3c Mutation	Double bit flip 	$S_m = 1/4$ $M = POP_s \times S_m$ $M_s = 1$
3d Compute fitness	Distance-based (with connectivity constraint for TPN), EDM average.	

c. *Mutation.* The number of mutants M is equal to the population size times a user-defined mutation occurrence ratio S_m. Mutants are randomly selected from the children generated in the previous step. The number of mutations per mutant (or mutation size) M_s is user-defined and represents the magnitude of the mutation. The algorithm then loops on each mutant m, and for each mutant loops on the number of mutations M_s per mutant. For each mutation, an index from Γ is randomly selected and replaced with an index corresponding to a non-channel location (i.e., double bit flip mutation). The mutation operation increases genetic diversity and thus reduces the risk of being trapped in a local minimum.

d. *Compute fitness.* The population is updated and fitness is re-calculated.

Results

Fast charging.— Permutation analysis.—Grid sizes from 4×4 to 8×8 were investigated, with the number of channels from 4 to 8 (surface coverage from 25 to 12.5%), that is a number of permutations from 1.8E3 to 4.4E9. The number of channels has been chosen specifically to compare with the grooved-line case (i.e., number of channel equals grid length so that a full line can be tested). Calculation times range from 6 s to 115 h. The genetic algorithm took only 18 s to converge for the largest grid with a population size of 1E4 individuals. Both methods achieve the same fitness, which validates the GA approach (albeit on a small grid). The only difference is that the permutation approach identified several equi-fitness optima due to problem symmetry, while the GA identified only one. Of main interest is the solution distribution of the permutation approach, plotted in Fig. 6. The worst case is the groove line, with the optimal pattern being $\approx$3 times more efficient. Most solutions are about two-times better than the grooved-line design, indicating that a random distribution has high probability to be much more efficient than grooved lines. The optimal pattern is a distribution of points far away from each other, thus subsequent

analyses for SPN are conducted using Eq. 4b instead of 4a to identify optimal disc channel pattern.

GA-based optimal distribution.—Figure 7 shows the optimal SPN disc-channel spatial distribution, along with the associated periodic EDM. The solution converged in around 100 iterations and reached a stopping criterion after 290 iterations. The wall-clock calculation time is 10 h on a single computer with a population size of 1E5 individuals. The spatial distribution that emerges seems to be a regular hexagonal pattern. Due to the inherent stochasticity associated with the GA-optimization approach, it is unlikely to reach the global minimum with a design space this large. This explains why the pattern is not an ideal regular hexagonal pattern, but an approximation. The fitness convergence (cf, Fig. 7c, and online supplementary video 1) also indicates that minor variations, which could be induced by a non-ideal manufacturing control, have minimal impact on the fitness. Fitness and channel spacing L_s (distance between nearest disc center L_{c-c} minus disc diameter w_c^t) as function of population size are also plotted in Fig. 8 to check the convergence. The analysis indicates fitness is slightly below 27.54 μm (to be compared with other patterns in the next paragraph), with a channel spacing slightly above 72.5 μm. The convergence toward a low standard deviation for the channel spacing indicates that the mono-objective optimization problem induces an indirect co-optimization: minimize distance heterogeneity, i.e., channel equidistance. This confirms that the converging pattern is a regular hexagon.

Comparison with random distribution and 1D-groove lines.—The fitness value calculated on the GA-optimized pattern does not provide information by itself, as there is no reference fitness value for an electrode without channels for SPN (unlike for TPN). Indeed, the distance map for SPN is the distance from an electrode material to the nearest channel. Without channels, it cannot be evaluated. For TPN, the distance can be evaluated even without channels as the domain's edges (electrolyte infiltration entry points) act as channels for the
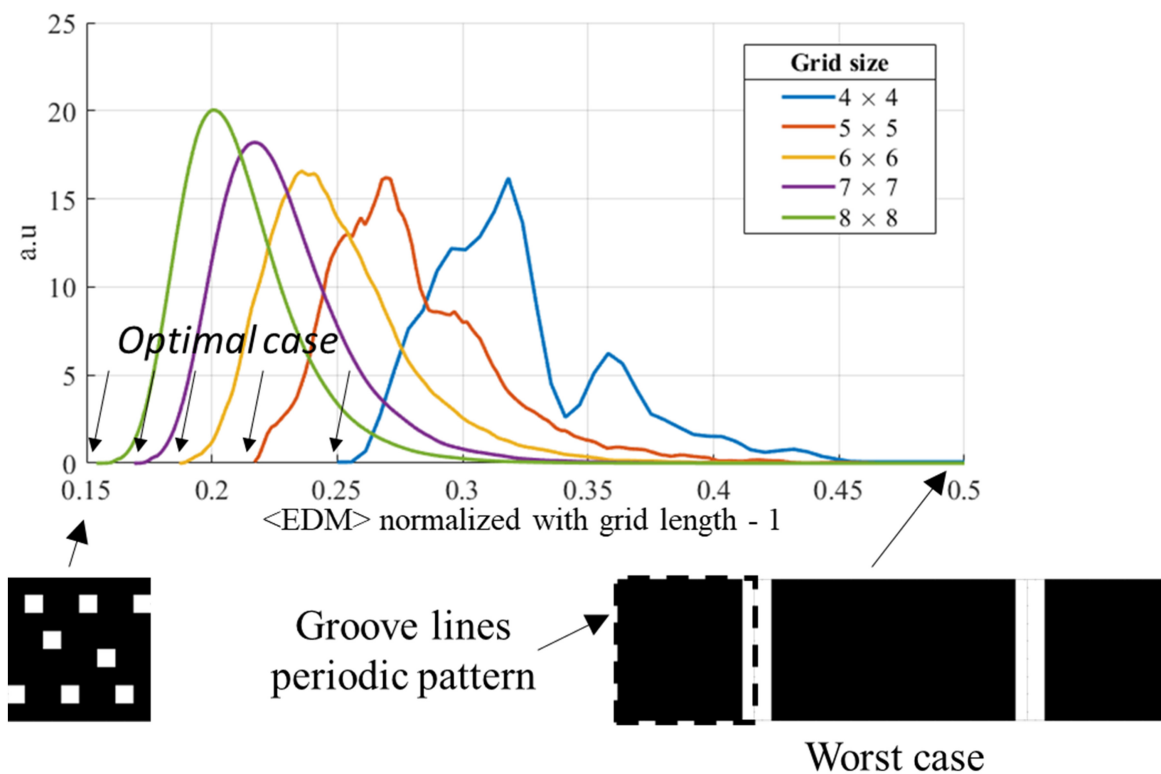

Figure 6. Fitness distribution function (all possible cases) calculated on a small gird without shape constraint. EDM has been used instead of *pEDM* for this particular analysis to reduce computational time.
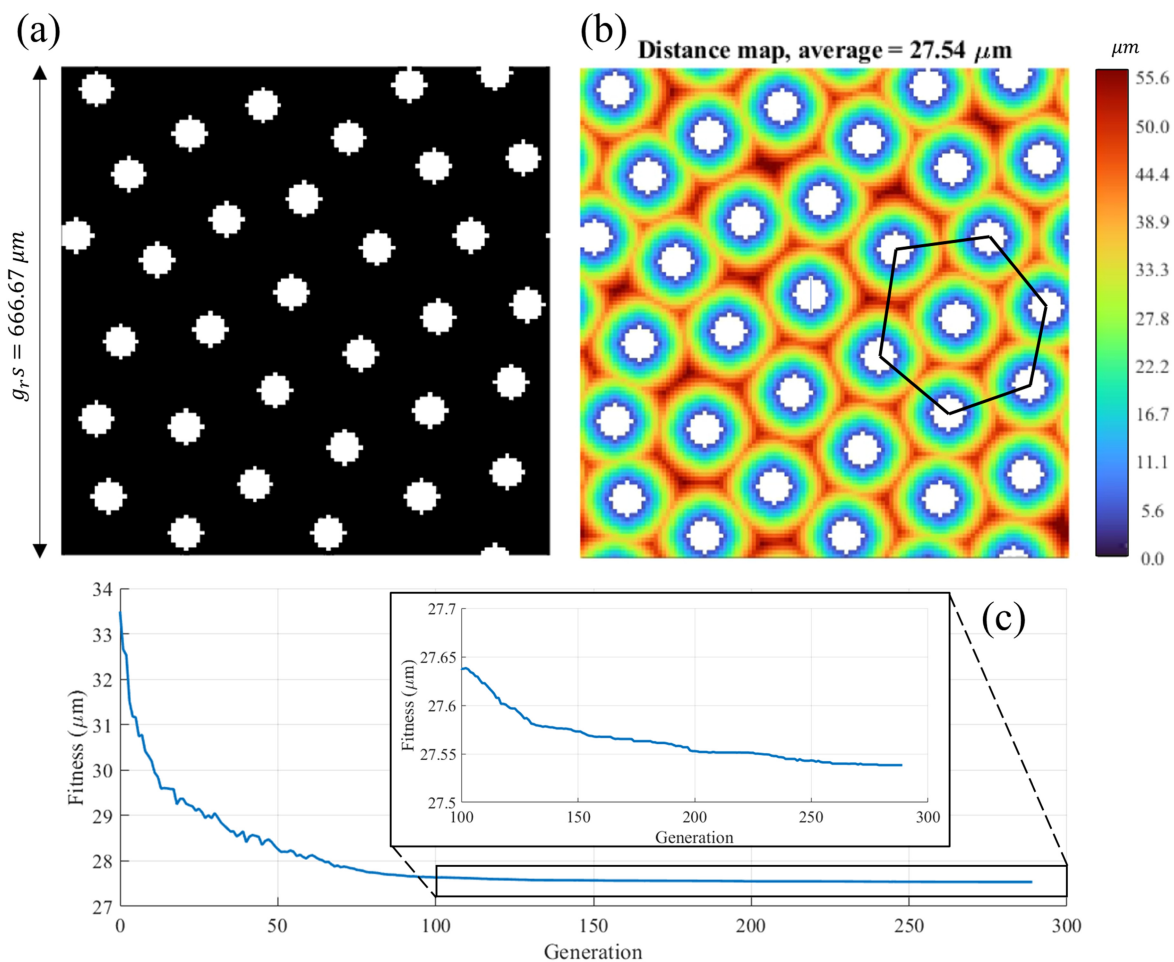
Figure 7. (a) Optimal SPN distribution, and (b) associated periodic Euclidean Distance Map (best individual is show). Solid lines represent an approximation of a regular hexagon pattern. (c) Genetic algorithm convergence with generation. Local fitness increase is due to the absence of an elitism operator. Convergence animation available online (supplementary video 1).
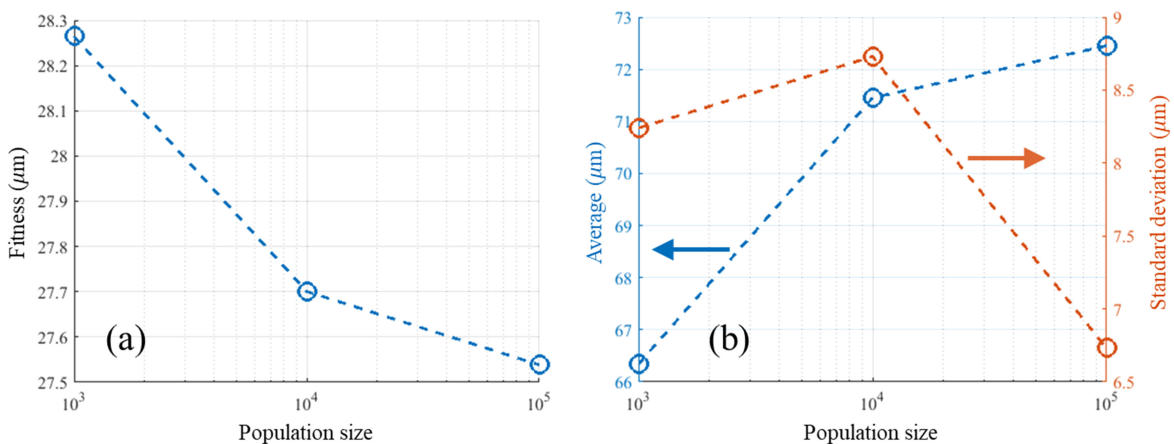

Figure 8. GA convergence with population size for (a) fitness and (b) channel spacing average and standard deviation.

fitness calculation. Therefore, a comparison is performed on two other patterns: grooved lines (considered as our baseline due to its simplicity and prevalence in the literature, cf, Fig. 9a and random distribution of disc channels (to test extreme case of poor manufacturing control, cf, Fig. 9b). Results are shown in Fig. 9. Fitness for the grooved-line pattern is calculated according to Eq. 6. Fitness for the regular hexagon pattern is numerically calculated on a very fine grid. The regular hexagon pattern has a lower fitness than the GA-

optimized pattern (cf, Figs. 9c–9d), in agreement with the population size convergence analysis (cf, Fig. 8). The grooved-line pattern appears to be strongly suboptimal, with regular hexagon pattern being ≈6.25 times more efficient. The random channel distribution provides a significant improvement, ≈3.5 times better than groove lines, and is only ≈1.8 times worse than the regular hexagon pattern; this demonstrates robustness in manufacturing laser ablated channels where, for example, if a high-throughput laser-ablation does not
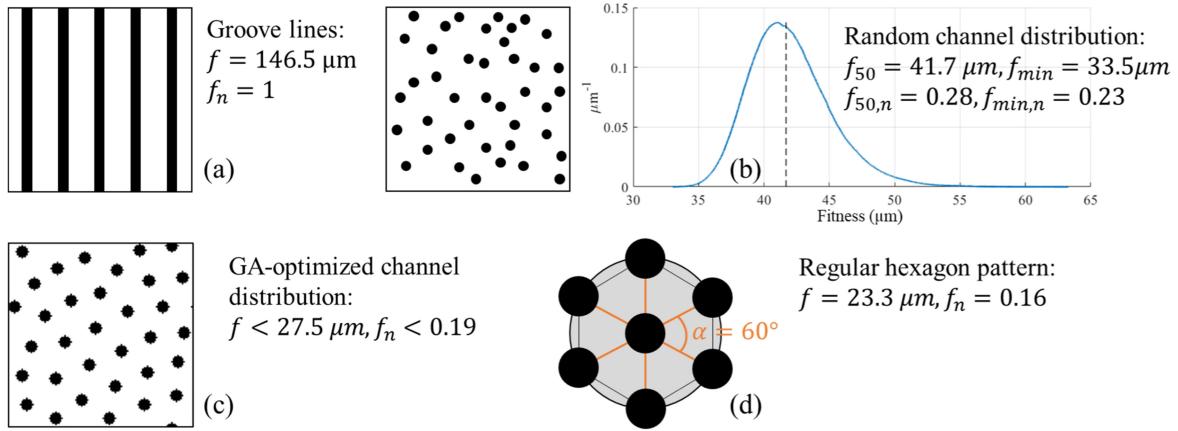
Figure 9. SPN fitness compared with, from worst to best: (a) groove lines, (b) random disc channel, (c) GA-optimized disc channel, and (d) regular hexagon disc channel. Normalized fitness with reference case (groove lines) is denoted f_n.

have good consistency in channel dimensions and placement, the cell's performance would be minimally impacted. Note these values are only relevant for the selected dimensions and channel volume.

Analytical relationship between channel volume, depth, and spacing.—Previous results clearly indicate that the regular hexagon pattern is the optimal one (cf, Fig. 7). With the geometric pattern known, we can derive analytical relationships linking channel volume ratio, channel dimensions, and channel spacing for both electrodes. We assume the distance between disc center L_{c-c} to be identical for both electrodes, so that the periodic domain has same dimensions. This implies the channel spacing L_s to be identical between electrodes (as both electrodes share the same disc diameter w_c^t). The cathode and anode baseline capacity (i.e., w/o channels) are known and noted $C_{b,c}$ and $C_{b,a}$, respectively. The dimensions will be deduced starting first with the anode, then with the cathode (the reader can modify the subscripts in the subsequent equations to go the other way). Three input parameters are required: the anode channel volume ratio $r_{V,a}$, the anode channel thickness $t_{c,a}$, and the N/P ratio for the structured cell N/P_s. The latter allows translating dimensions from one electrode to the other. The anode channel volume and the anode volume within the regular hexagon periodic pattern, respectively $V_{c,a}^p$ and V_a^p, are calculated according to Eqs. 9a and 9b. The notations from Eq. 1a are re-used, with an additional subscript to identify the electrode. The distance between disc center L_{c-c} is deduced knowing the anode channel volume ratio $r_{V,a}$ using Eq. 9c. Channel spacing L_s is deduced with Eq. 9d.

$$V_{c,a}^p = \left(\frac{1}{6} + \frac{1}{12}\right) V_{c,a} \qquad [9a]$$

$$V_a^p = \frac{t_a L_{c-c}^2 \tan(60°)}{8} \qquad [9b]$$

$$r_{V,a} = \frac{V_{c,a}^p}{V_a^p} \text{ then } L_{c-c} = \sqrt{\frac{8 V_{c,a}^p}{t_a\, r_{V,a} \tan(60°)}} \qquad [9c]$$

$$L_s = L_{c-c} - w_c^t \qquad [9d]$$

On the cathode side, the channel volume ratio is deduced from Eqs. 10a–10c, with $C_{s,a}$ and $C_{s,c}$, respectively, the anode and cathode capacity after structuring. Equation 10d (from re-writing of Eq. 9c) is used to deduce the cathode channel volume within the regular hexagon periodic pattern $V_{c,c}^p$. Cathode channel volume $V_{c,c}$ is deduced by inversing Eq. 9a, cf. Eq. 10e. Channel bottom volume

$V_{c,c}^b$ is deduced knowing the full cone volume $V_{c,c}^{max}$ (cf, Eq. 1a) according to Eq. 10f. Equation 1a is re-ordered to provide the difference between the cone maximum thickness $t_{c,c}^{max}$ and the channel actual thickness $t_{c,c}$, cf, Eq. 10g. The cathode channel thickness is deduced with Eq. 10h. Note that an irrelevant N/P_s can lead to no solution (negative length).

$$C_{s,a} = C_{b,a}(1 - r_{V,a}) \qquad [10a]$$

$$C_{s,c} = \frac{C_{s,a}}{N/P_s} \qquad [10b]$$

$$r_{V,c} = 1 - \frac{C_{s,c}}{C_{b,c}} \qquad [10c]$$

$$V_{c,c}^p = \frac{r_{V,c}\, t_c\, L_{c-c}^2 \tan(60°)}{8} \qquad [10d]$$

$$V_{c,c} = V_{c,c}^p / \left(\frac{1}{6} + \frac{1}{12}\right) \qquad [10e]$$

$$V_{c,c}^b = V_{c,c}^{max} - V_{c,c} \qquad [10f]$$

$$\Delta = t_{c,c}^{max} - t_{c,c} = \sqrt[3]{\frac{3 V_{c,c}^b \tan(\theta_c)^2}{4\pi}} \qquad [10g]$$

If Δ real number, then $t_{c,c} = t_{c,c}^{max} - \Delta$, otherwise no solution
$$[10h]$$

Considering the channel dimensions and capacities of the electrode investigated (cf, Table I), the parameter space is plotted in Fig. 10 for two N/P_s. This defines the parameter space that an electrochemical model could investigate to find an optimum SPN pattern for fast charging.

Fast wetting.—Case-specific nomenclature for the different TPN patterns used in this section (e.g., "GA-C-8") is available in Fig. 2.

Coin-cell form factor.—The GAs convergence was investigated, with pixels per diameter of the coin cell disk from 80 to 200, and population size from 5E3 to 5E4, respectively, to accommodate for the larger design space. Analysis indicates near convergence for cumulative channel length, from 7.91 to 7.97 cell-unit diameter
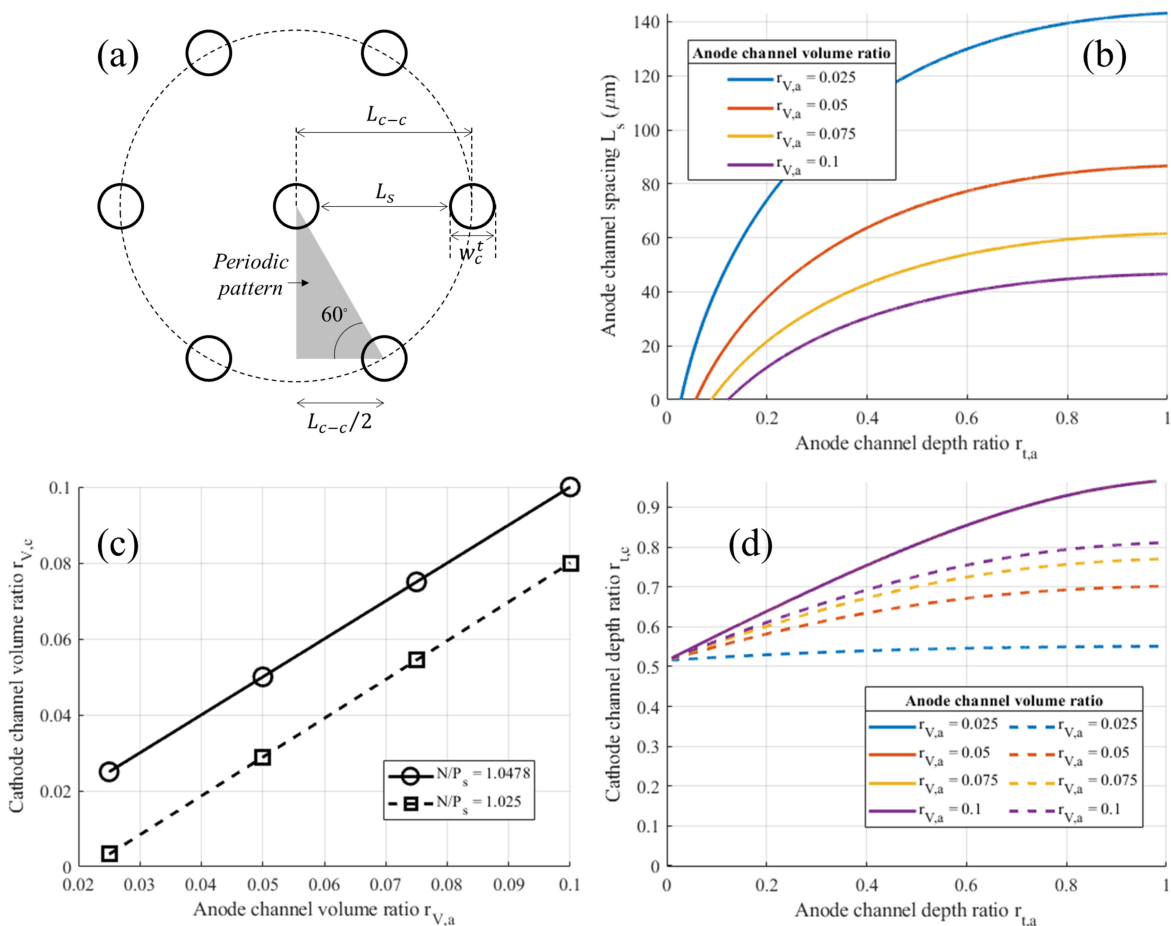
Figure 10. Pore Network parameter space for optimal pattern regular hexagonal for electrode specifications of Table I. (a) Regular hexagonal pattern, (b) anode channel spacing, (c) cathode channel volume ratio, and (d) cathode channel depth ratio (all solid lines, $N/P_s = N/P_b$ case, overlap). Input geometric parameters are anode channel volume ratio $r_{V,a}$ and anode channel depth ratio $r_{t,a}$ (defined, respectively in Eqs. 1c and 1a), and N/P ratio for the structured cell. (c,d) Solid line is $N/P_s = N/P_b$, dashed line is $N/P_s < N/P_b$.

(area-based), and from 10.98 to 10.92 cell-unit diameter (effective-length based, cf, Fig. 3) and slight overestimation for normalized fitness, from 0.129 to 0.116, for GA-C-8 (nomenclature illustrated in Fig. II). Subsequent results correspond to the most refined case. Calculation time for the most refined case was two weeks on a 10-core computer.

The TPN patterns identified with the GA-optimization approach are plotted in Fig. 11, top row. All pixels assigned to the channel domain are connected to the cell edges. For a low number of equivalent channel diameter (GA-C-4), the pattern is roughly radial with minor branching. However, as more channels are introduced the radial component is less obvious, in favor of a mud-crack-like pattern with branching being the dominant feature (GA-C-16). No symmetry is visible due the inherent stochasticity of the method, however the mud-cracking pattern is seemingly repeated uniformly within the whole cell domain, especially for the case with a higher number of channels. A similar pattern at equivalent radial distance was expected due to the isotropy of the problem. This suggests that the population size is high enough to capture the expected trend.

The pattern is however not uniform if analyzed branch-wise or channel-wise ("channel" here being defined as branch and sub-branches all connected to each other), with two characteristics visible. First, the branching increases from the electrolyte infiltration entry-edges to the center of the cell (cf, Fig. 11, GA-C-8, numbers). Subbranches are typically generated perpendicular to their parent branch to cover the most area possible without using a full branch from the electrolyte infiltration edge. Such behavior is also visible in diffusion-problem topology optimization (cf, Fig. 6 of Refs. 54 and

55). Second, the connected channel length is alternating (roughly, as stochasticity induces some variations), with the general pattern being one small channel between two larger channels (i.e., small-large-small-large-small etc., modulo stochasticity, cf, Fig. 11, GA-C-8, letters). This behavior is a consequence of the curvature of the coin-cell domain geometry: as perimeter is smaller near particle center, less branches are required to cover the same amount of cell surface. This was the main idea behind the clock pattern, and it is remarkable that the GA reproduced this general pattern without explicit constraint. The optimal pattern is thus a combination of channel length alternation with increasing perpendicular branching from cell edge to center. The channel length alternation provides the periodic pattern. However, as more channels are generated with the number of equivalent channel diameter, this implies the periodic pattern length is not constant. Using periodic boundary condition to reduce the problem size is thus not a good idea as it requires *a priori* knowledge of the solution to generate.

Figure 12 shows normalized fitness for the pre-determined patterns used for comparison. With no grid resolution limitation, and known equivalent diameter (i.e., near zero numerical error), the order from best to worst is clock, then radial and branch with similar fitness, and then circle (cf, Fig. 12a). It could be surprising that the branch pattern is suboptimal, since patterns identified with the GA are strongly branching. However, making a branch pattern manually is very likely to be suboptimal as sub-branching implies a very large parameter space, which results in this pattern underperforming. The clock pattern is optimal among the pre-determined patterns in agreement with the feature (channel length alternation) identified
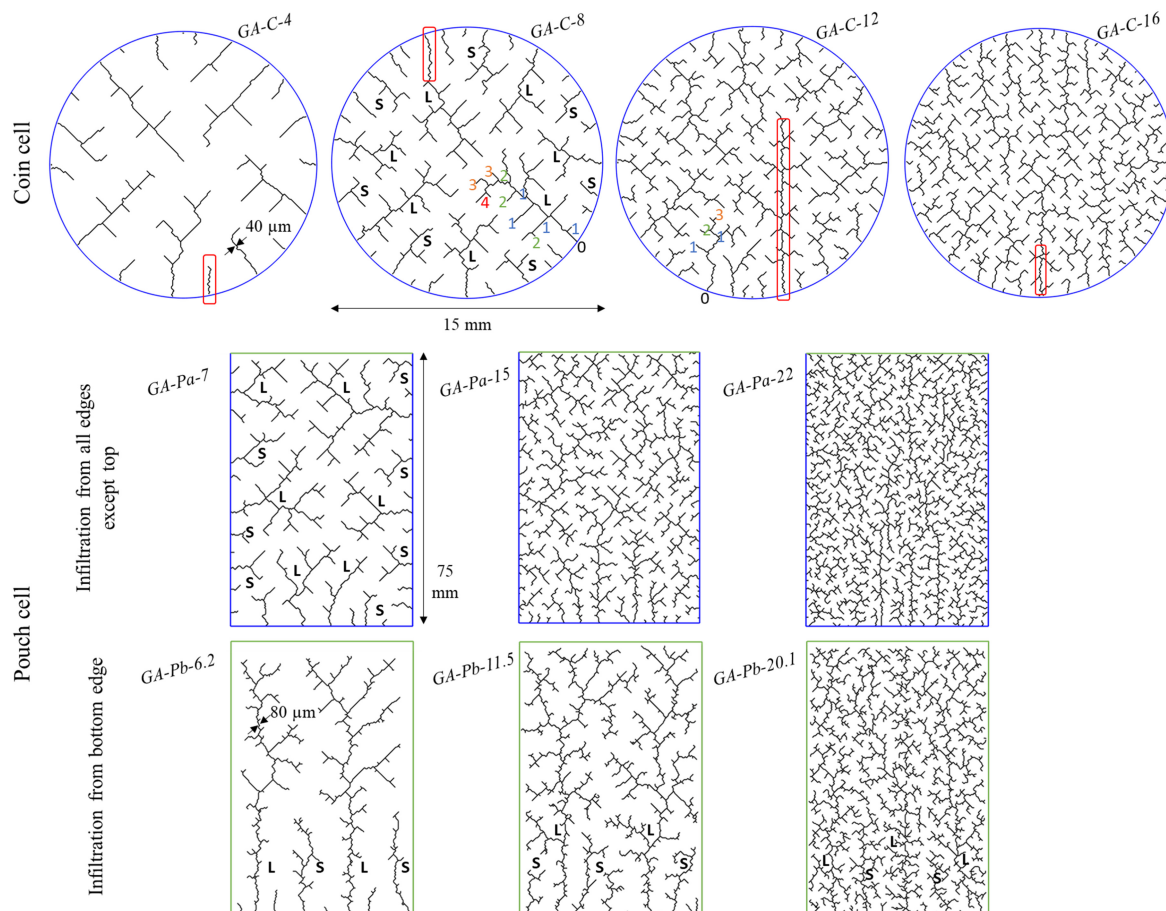
Figure 11. TPN Optimal patterns identified with the GA-optimization approach for (top) coin cell and (bottom) pouch cell. Channel width is not scaled with cell dimension. Blue lines indicate the electrolyte infiltration entry-edges, green lines, if any, indicate cell edges without infiltration. Numbers indicates the branching number (starting at 0 for the initial parent or main branch), letters S, L indicate a short and a long connected channel. Red rectangle indicates irrelevant zig-zag patterns induced by the stochasticity inherent with the GA-optimization approach. Convergence animation available online (supplementary video 2).

with the GA-optimization approach. Very significant gains (5–10 times better than the no-channel case) are achieved with a minor electrode volume loss (1%-2%), thus allowing to couple a TPN (≈1.5%) with a SPN (≈5%) for a total volume loss of ≈6.5%. Furthermore, the fitness reduction (i.e., the slope) is decreasing with the number of equivalent diameters, indicating the better trade off fitness-volume loss is achieved for the low volume loss range.

Comparison analysis between pre-determined patterns and patterns identified with the GA-optimization approach are performed at same grid resolution (i.e., 200 pixels per diameter) and results are show in Figs. 12b and 12c. Furthermore, the cumulative length metrics are calculated identically between the different patterns for a fair comparison, with the method explained in the *Simpler patterns and comparison methodology* section. Note that both comparison metrics (area-based and effective length-based) have their benefits and drawbacks. The area-based comparison represents real channel surface coverage if pixel size and channel size match, but then in this case, the connectivity requirement should be face-to-face, thus strongly limiting the channel shape and eventually biasing the analysis. Furthermore, the area-based metric does not distinguish horizontal or vertical channels from diagonal channels even though their true length is different from a factor $\sqrt{2}$. Effective-length comparison relaxes the constraint of the connectivity requirement with diagonal being correctly measured and is a relevant solution for the pixel size channel size mismatch (cf, Fig. 3). However, the effective-length metric penalizes (increases) the real channel length of the patterns identified with the GA. Indeed, due to the

stochasticity of the GA-optimization approach, what would be otherwise a straight line is sometimes represented with a zig-zag of 1–2 pixel with (cf, Fig. 12, red rectangles). In both comparative approaches, the GA patterns have lower or equal fitness compared with the best choice (clock) among the predetermined patterns. It is then believed that the GA curve of Fig. 12c is over-translated toward the high length due to the zig-zag penalty discussed above, thus penalizing it against the pre-determined patterns.

Analysis of the EDMs reveal the reason behind the better performance of the patterns identified with the GA-optimization approach. For patterns with similar channel area (labelled in Fig. 12b), the EDM distribution function is narrower for GA patterns, indicating a more equidistant distribution of the channels (cf, Fig. 13). This is also noticeable from visual inspection of the EDM: radial and branch patterns have larger distance near cell edges, clock patterns have larger distance near cell center, while GA patterns have a very uniform distribution. Note that these trends are intrinsic to the patterns investigated and stand for different channel density. The GA demonstrates here its superiority by uniformizing the porous matrix-to-channel distance, as the indirect product, or co-optimization, of minimizing the average porous matrix-to-channel distance.

Pouch cell form factor.—The grid used for the genetic algorithm is 150 by 225 with a population size of 5E4. The TPN patterns identified with the GA-optimization approach are plotted in Fig. 11, middle (electrolyte infiltration from all edges except top one, case *a*)
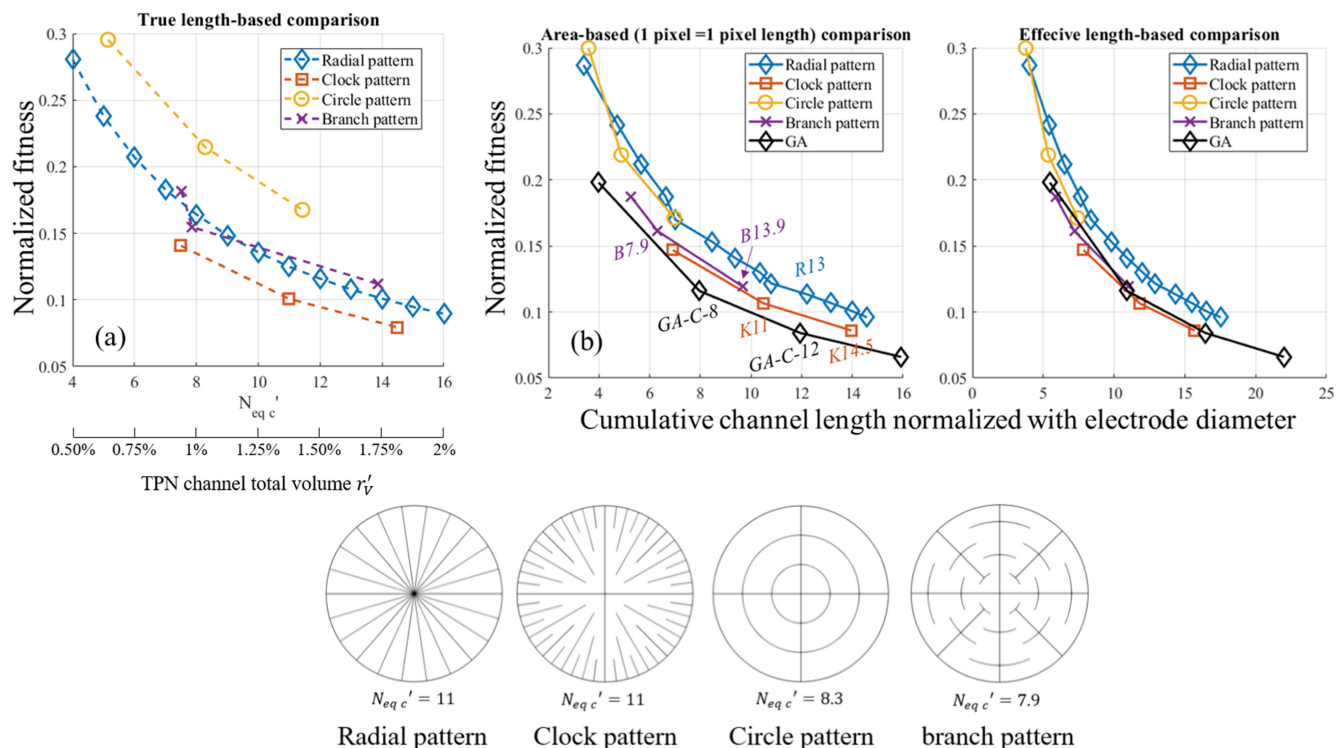
Figure 12. TPN patterns comparison for coin cell. (a) Pre-determined pattern with near-infinite grid resolution (2000 pixel per diameter). Equivalent number of diameter $N_{eq\,c}'$ and channel total volume r_v' are known. (b, c) Comparison on a finite grid (200 pixel per diameter), with (b) area-based comparison, i.e., one pixel = one pixel length, and (c) effective-length comparison (cf, Fig. 3). Radial, clock, circle and branch patterns from Fig. 2 are reminded in the bottom for convenience.

and bottom (electrolyte infiltration from bottom edge, case *b*) row. For the relatively low channel volume, patterns are different between the two electrolyte infiltration modes with dominantly vertically aligned channel for the case *b* (e.g., Fig. 11 GA-Pb-6.2) and both horizontally and vertically aligned channel for the case *a* (e.g., Fig. 11, GA-Pa-7). For the higher channel density cases, the differences between the two cases are vanishing. This is the consequence of the subbranches being typically perpendicular to their parent branch. Indeed, with a limited number of channels, the initial orientation of the branches from the edges, controlled by the electrolyte infiltration mode, is the dominant orientation. However, with higher channel density, the sub-branching mechanism is becoming predominant, and the cumulated perpendicular branching leads to an apparent channel orientation isotropy with only a loose correlation with the electrolyte infiltration mode. While vertical channels appear in general longer than their horizontal counterparts, this is believed to be induced by the cell aspect ratio with a longer vertical dimension. Overall, the optimal pattern predicted shares the same characteristics with the coin cell case: channel length alternation and increasing perpendicular branching from electrolyte infiltration edge to bulk of the cell. These two features are particularly visible for the low-density channel cases (cf, Fig. 11 GA-Pa-7 and GA-Pb-6.2). The channel length alternation in case *b* is however not induced by curvature which indicates this feature is intrinsic with the optimal TPN pattern (while being still controlled partly by the form factor as explained for the coin cell case). Such a feature is derived from the perpendicular branching: a sub-branch from a channel will reduce the distance in the area that would have been covered otherwise by the adjacent channel thus limiting the required length and branching of the latter.

Figure 14 shows the normalized fitness for the pre-determined patterns used for comparison. With no grid resolution limitation and a known number of channels, a lower normalized fitness has been calculated for the case b (infiltration from bottom edge, cf, Fig. 14a).

While this could appear counter-intuitive (as the case with more electrolyte infiltration entry edges has higher normalized fitness), this is due to the difference on the baseline fitness. Indeed, baseline fitness is significantly higher for the case *b* (3.37 times higher than case *a*), while the impact of the electrolyte infiltration mode on structured fitness only impacts the two vertical edges of the cell. This means that the absolute fitness calculated for structured pouch cell with the two electrolyte infiltration modes is roughly similar (minor an edge effect) with better value for the case *a*, but the initial fitness is much worse when electrolyte is allowed to infiltrate only from the bottom edge. Both cases should be considered as extremums, with electrolyte infiltration only from the bottom edge being the conservative (only true in the initial part of the infiltration process, and possibly also near the end, when the majority of the electrolyte has already penetrated into the electrodes and the liquid level in the cell drops) and electrolyte infiltration from all edges except the top is a more optimistic case (initially incorrect with relevance increasing as the infiltration progresses). Both cases are a simplification as Habedank et al.[8] demonstrated electrolyte penetration from three sides, but with a faster penetration from the bottom than from the sides. Similarly with the coin cell form factor, very significant gains (∼20 times better than the no-channel case) are achieved with a minor electrode volume loss (1%). Additionally, the fitness reduction is mainly achieved for the low volume loss (<1%) indicating there is no need to sacrifice more active material.

Comparison between the vertical pattern and patterns identified with the GA-optimization approach are performed at same grid resolution (i.e., 150 pixels along cell width) and results are show in Figs. 14b and 14c. The larger cell dimension of the pouch cell as compared to the coin cell significantly degrades the GA precision. Indeed, to achieve a 1:1 scale between pixel length and channel width in the coin cell case 11.0E4 pixels are required, while GA grid used 3.1E4 pixels (≈3.5 times less). In the pouch cell case 58.6E4 pixels are required, while GA grid used only 3.4E4 pixels (≈17.4
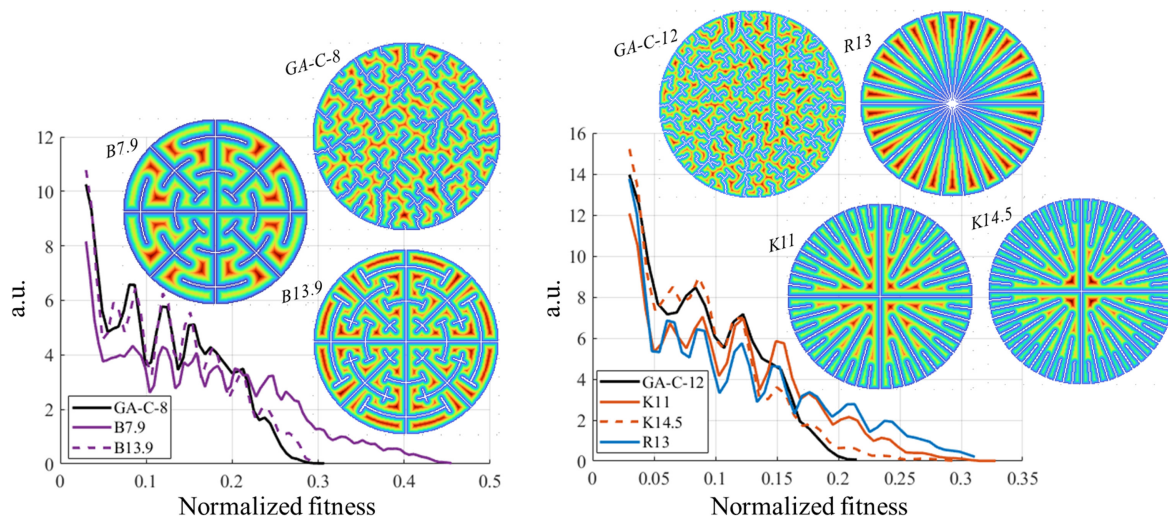
Figure 13. Coin cell TPN EDM and associated normalized fitness distribution. (Left) GA-C-8 compared with B7.9 and B13.9, and (right) GA-C-12 compared with R13, K11 and K14.5.
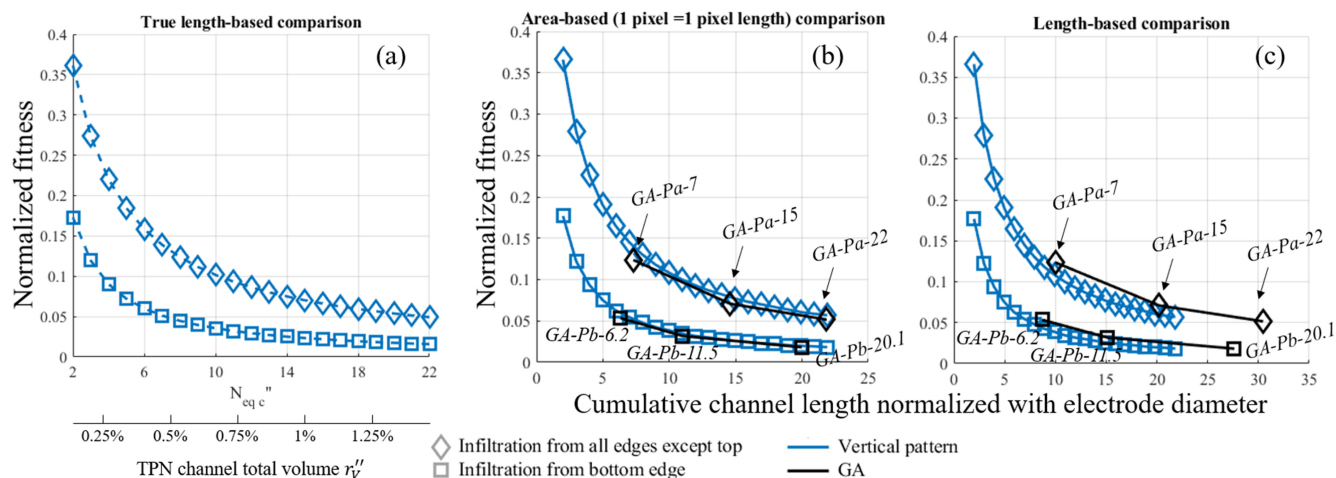

Figure 14. TPN patterns comparison for pouch cell. (a) Pre-determined pattern with near-infinite grid resolution (2000 pixel along cell width). Equivalent number of vertical channels $N_{eq\,c}''$ and channel total volume r_v'' are known. (b, c) Comparison on a finite grid (150 pixels along cell width), with (b) area-based comparison, i.e., one pixel = one pixel length, and (c) effective-length comparison (cf, Fig. 3).

times less). Because of this, the GA pattern predicted with the limited grid are suboptimal as the amount of sub-branching is limited by the grid resolution. In comparison, the deterministic patterns are only moderately impacted by the grid resolution as all details are described whatever the resolution. Therefore, Figs. 12b, 12c but especially Figs. 4b, 4c are not "fair" comparisons between the predetermined and GA-optimized patterns (in addition to the zig-zag penalization discussed for the coin cell form factor). For the pouch cell case, the aim of the figure is then primarily to show that most gains are achieved with a low channel volume as for the vertical patterns.

Discussion

On the method.—The GA-optimization confirmed that the hexagonal pattern is optimal for fast charging, providing further confidence to the patterns found in litterature[4,10,22,24] albeit with a lack of clear justification and sub-optimal pitch between channels. Beyond the pattern identification, the added value is to validate the GA-optimization approach ability to perform such topology optimization for a diffusion/distance problem, even for a periodic/regular pattern, such as regular hexagon, that a stochastic-based approach

may have been ill-suited for. This builds confidence in the subsequent TPN analysis, for which the optimal is not known. Furthermore, the ability to identify regular patterns suggests that the GA discarded the straight lines patterns (radial, clock) not because it cannot investigate them due to its stochastic approach (population size is not infinite) but because it identified them as suboptimal, although not far from it. To support this statement, the GA did generate some roughly straight/diagonal lines when needed to reach an optimum (cf, Fig. 11).

One interesting aspect of GA lies in its apparent simplicity. Unlike other optimization approaches that are mathematics-heavy, GA is much more intuitive. Furthermore, tuning the method proved to be simple: a few quick tests were enough to identify a parent selection threshold of 1/4 as efficient. Then, the only parameter to change to achieve convergence for different grid size was the population size. Similarly, while a faster convergence may have been achieved with more time dedicated to test different methods for the GA operators (parent selection, crossover, mutation),[34] the simple truncation, one point crossover, and bit flip operators were enough for the task. This makes this method a good candidate for easy-to-implement, prototyping optimization, which is the outcome of this work: identifying (adimensional) optimal patterns and

narrowing down the associated physical dimension optimal range by using a CPU-cheap fitness function compatible with thousands of calculations, while being correlated with the electrochemical gain expected by the channels' introduction.

On the uncoupled SPN and TPN approach.—While it would have been possible to run the GA with both SPN and TPN objective functions, this would have required to weight each of them or use a Pareto front. Specifically, the unconnected channels that only benefit SPN would have contributed less to the fitness function compared to the connected channels that benefit both SPN and TPN. Determining such weights is arbitrary and depends on the application, and thus has not been done in this work. For instance, a cell designed for stationary storage and/or low charge rate and/or low thickness does not need a SPN as it is unlikely to be transport-limited, while still benefiting from the manufacturing cost reduction provided by the lower drying time offered by TPN. Furthermore, the TPN provides mainly a one-time cost-reduction, while the SPN provides mainly an in-operation performance improvement for otherwise transport-limited cells, making a relevant weighting difficult for such different metrics. In this work, we choose to investigate each network distinctly to identify their respective features without convoluting them. This choice is *a posteriori* made even more relevant in regards with the significant difference between SPN and TPN channel volume required to provide significant improvements for their respective fitness functions. SPN required much more volume (5% induced a 6 times improvement) compared to TPN (1%-2% induced a 5–20 times improvement), roughly 5 to 10 times higher impact at equivalent volume. This indicates that, for SPN and TPN channels with similar diameters and widths, a combined SPN and TPN pattern would consist in relatively few TPN channels far apart from each other, with relatively more SPN channels located in between TPN channels. That is essentially a superposition of the two patterns, which matches well with an independent analysis as done in this work. Such mixed patterns, experimentally achieved in our laboratory in a roll-to-roll high throughput process, will be the subject of a future article.

On the results.—Optimal channel width w_c^t is specified for SPN (the smallest diameter allowed by the laser system, to a certain extent). However, picking the channel width for TPN is less evident due to fluid dynamics considerations: channel width is expected to decrease from electrolyte infiltration entry-edges to the cell bulk.[55,56] The channel widths selected for TPN are then a combination of numerical consideration and laser system limitations, but not the optimal value. Because of this, physical dimensions in the TPN pattern are not optimal values since one dimension (channel width) is user-defined. However, the overall pattern shape is still recommended, i.e., without physical length attached, but from an adimensional perspective.

Dimensions within the SPN pattern are, however, expected to be a good approximation of the real optimum, and an electrochemical model can further refine this by analyzing a parameter space near the GA optimum. While it is very likely that the fitness is negatively correlated with the electrochemical gains induced by the channels (as SPN have been originally introduced based on diffusion distance consideration), it is unlikely such correlation is linear. This implies the trade-offs, at fast charge, between volume loss to fitness reduction and volume loss to capacity improvement evolve differently as volume loss increases, resulting in a different practical optimum. Additionally, the physics-less approach used in this work makes it not worth the extra-CPU time required to push the grid resolution to a 1:1 scale between channel width and pixel length, especially for the TPN. The main result is the overall pattern shape (increasing resolution would only add even more sub-branching) and information that only 1%-2% volume loss is required for TPN.

A general comment on the patterns identified with the GA-optimization approach is that while the overall shape is believed to be indeed the optimum shape, local shape is however suboptimal due to the inherent stochasticity of the method. An example of such local

approximation is the numerous one-voxel width zig-zag patterns (cf, Fig. 11), that have also the side effect to make comparison with pre-determined patterns less accurate. However, the branching generated by the GA is believed to not to be an artifact from the method stochasticity but a true feature of the optimal pattern. Such a statement is supported by the subbranch length, which is much longer than a few pixel lengths which suggests stochasticity is not involved, and by the literature that also points toward branching patterns.[54,55] Furthermore, if stochasticity was to bias the pattern, then significant variations would have arisen locally. Instead, the pattern predicted by the algorithm is very uniform from one region to the next, especially at high channel density (cf, Fig. 11, GA-C16, Ga-Pa-22 and Ga-Pb-20.1) with repeating features such as channel length alternation and perpendicular sub branching.

The results presented in this work only consider half-depth channels for simplicity (i.e., $r_t = 0.5$). If the channel thickness ratio is changed, the optimal patterns would still be the same overall, but the channel surface coverage will be denser or coarser at equivalent channel volume. Also, the unknown correlation between the electrochemical performance metrics and the distance-based fitness function will be different. Ideally, the remaining thickness below the channel should be adjusted (using equations in *Analytical relationship between channel volume, depth, and spacing* section for SPN) until the characteristic diffusion time for the remaining through-plane diffusion below the channel (characteristic diffusion distance: $t_e - t_c$) would be similar with the characteristic in-plane diffusion time between channels (characteristic diffusion distance: $L_s/2$) so that electrode material would be equally transport-limited in both directions (diffusion anisotropy is to be considered for the calculation of the through-plane and in-plane characteristic diffusion time). This means that for thicker electrodes, increasing the channel thickness ratio is likely to be required, thus de-densifying SPN channels (i.e., lower surface coverage) at equivalent channel volume.

Feasibility for practical implementation.—SPNs and TPNs can be implemented by loading the pattern into the software of the laser system as a catalog (.cat) file, for example. Femtosecond laser systems have been shown to introduce patterns without any significant unfavorable material damage or loss in cycle-life performance.[5] The complexity of the pattern introduced in a roll-to-roll laser ablation arrangement only marginally increases the technical challenge of implementation. For example, straight lines may only require the use of diffractive optical element beam splitters and constant power applied on the moving sheet, while more complex patterns would require more advanced optics such as polygon systems and additional programming to optimize the sequence and location of laser pulses on the sample. Some 2D patterns, such as the regular hexagonal pattern (optimal SPN), can also be achieved, or approximated, using the equipment required for straight lines, simply by turning on and off the laser or opening/closing a shutter to produce dashed lines. Both simple and complex patterns are expected to be feasible on roll-to-roll assembly lines. Demonstrating roll-to-roll laser ablation will be the focus of a future manuscript by our team at the National Renewable Energy Laboratory (NREL).

Applications for future use.—As laser ablation becomes adopted in commercial scale manufacturing, a method to quickly identify the optimal pattern for a given single or set of fitness functions will be needed. This is particularly important since the implementation of complex patters to achieve a variety of distinct or combinations of goals such as fast charging, fast wetting, and relief of mechanical strain in electrodes with high volumetric expansion, will be needed. Optimization of the complex patterns for their set of fitness functions will require such a computationally efficient approach as the GA demonstrated here. Femtosecond laser ablation hardware is capable of complex patterns for high throughput roll-to-roll processing thanks to the availability of high power (>300 W) femtosecond lasers and extremely fast-moving optics systems such as polygon scanners, but computational approaches to help guide microstructure patterns remain elusive. A perspective on hardware limits for scaling

laser ablation to >100 m min^{-1} roll-to-roll processing will be provided in future work, while this work focuses on how researchers and engineers can use an accessible and efficient approach to achieve pattern optimization and is expected to accelerate first-time-right approach to manufacturing.

Conclusions

Secondary and tertiary pore network channel optimal spatial distribution patterns have been identified, respectively, for fast charging and fast wetting using a distance-based optimization approach relying on an in-house genetic algorithm. The GA has been first validated on a small grid and has been found thousands of times faster than the permutation-based, brute force, approach. The model predicts disc-shape channels arranged in a regular hexagonal pattern is optimal for fast charging, and associated SPN dimensions were provided considering technical constraints of the laser system. Improvements induced by the regular hexagonal pattern were compared with the simpler grooved-lines pattern, with the latter being found to be strongly sub-optimal ($\sim$6.25 times less efficient for an equivalent arbitrary chosen 5% electrode volume loss). Minor variations from the optimal pattern had minimum impact on the calculated fitness, indicating that non-ideal manufacturing control would not significantly degrade the expected performance improvements. For fast wetting, the model predicts that a mud-crack-like pattern is optimal to reduce electrolyte infiltration distance, with channel length alternation and increasing perpendicular branching, from the infiltration edges to the cell center, being the two main features. The optimal pattern is influenced by the cell form factor (coin cell, pouch cell) and the electrolyte infiltration entry-edges only for low TPN channel volume ($<$1% electrode volume), but then transition indifferently to the above-mentioned generic mud-crack-like pattern for higher channel volumes. Improvements induced by the mud-crack-like pattern were compared with simpler, easier to manufacture, pre-determined patterns. The "clock" pattern (radially oriented channels with alternating length) was predicted to be the most efficient among the investigated designs (except for the GA-optimized pattern). For all the TPN patterns (both pre-determined and GA-optimized) and all the cell form factors investigated, very significant gains (5–20 times better as compared to the no-channel case) were achieved with a minor electrode volume loss (1%–2%), with only marginal gains obtained afterwards. The model then predicts significant improvements can be expected, respectively, for fast charging compared with grooved lines, and for fast wetting compared to no-channels, by sacrificing only a limited electrode volume (7% in total).

ORCID

Francois L. E. Usseglio-Viretta https://orcid.org/0000-0002-7559-8874

Peter J. Weddle https://orcid.org/0000-0002-1600-0756

Bertrand J. Tremolet de Villers https://orcid.org/0000-0001-8685-539X

Nathan Dunlap https://orcid.org/0000-0002-9002-9602

Dana Kern https://orcid.org/0000-0003-0814-8723

Kandler Smith https://orcid.org/0000-0001-7011-0377

Donal P. Finegan https://orcid.org/0000-0003-4633-560X

References

1. A. M. Colclasure, A. R. Dunlop, S. E. Trask, B. J. Polzin, A. N. Jansen, and K. Smith, *J. Electrochem. Soc.*, **166**, A1412 (2019).
2. J. Park, S. Hyeon, S. Jeong, and H.-J. Kim, *J. Ind. Eng. Chem.*, **70**, 178 (2018).
3. J.-H. Rakebrandt, P. Smyrek, Y. Zheng, H. J. Seifert, and W. Pfleging, *Proc. SPIE 10092, Laser-based Micro- and Nanoprocessing XI* (2017).
4. J. B. Habedank, J. Kriegler, and M. F. Zaeh, *J. Electrochem. Soc.*, **166**, A3940 (2019).
5. N. Dunlap et al., *J. Power Sources*, **537**, 231464 (2022).
6. D. L. Wood III, J. Li, and C. Daniel, *J. Power Sources*, **275**, 234 (2015).
7. W. Pfleging and J. Pröll, *J. Mater. Chem. A*, **2**, 14918 (2014).
8. J. B. Habedank, F. J. Günter, N. Billot, R. Gilles, T. Neuwirth, G. Reinhart, and M. F. Zaeh, *Int J Adv Manuf Technology*, **102**, 2769 (2019).
9. F. L. E. Usseglio-Viretta, W. Mai, A. M. Colclasure, M. Doeff, E. Yi, and K. Smith, *Electrochim. Acta*, **342**, 136034 (2020).
10. Y. Kim, A. Drews, R. Chandrasekaran, T. Miller, and J. Sakamoto, *Ionics*, **24**, 2935 (2018).
11. L. Hille, M. P. Noecker, B. Ko, J. Kriegler, J. Keilhofer, S. Stock, and M. F. Zaeh, *J. Power Sources*, **556**, 232478 (2023).
12. J. Kriegler, L. Hille, S. Stock, L. Kraft, J. hagemeister, J. B. Habedank, A. jossen, and M. F. Zaeh, *Appl. Energy*, **303**, 117693 (2021).
13. K.-H. Chen et al., *J. Power Sources*, **471**, 228475 (2020).
14. C. Zwahr, N. Serey, L. Nitschke, C. Bischoff, U. Rädel, A. Meyer, P. Zhu, and W. Pfleging, *Int. J. Extrem. Manuf.*, **5**, 035006 (2023).
15. M. Yamada, N. Soma, M. Tsuta, S. Nakamura, N. Ando, and F. Matsumoto, *Int. J. Extrem. Manuf.*, **5**, 035004 (2023).
16. W. Mai, F. L. E. Usseglio-Viretta, A. M. Colclasure, and K. Smith, *Electrochim. Acta*, **341**, 136013 (2020).
17. C. L. Cobb and S. E. Solberg, *J. Electrochem. Soc.*, **164**, A1339 (2017).
18. R. Dubey, M.-D. Zwahlen, Y. Shynkarenko, S. Yakunin, A. Fuerst, M. V. Kovalenko, and K. V. Kravchyk, *Batteries and Supercaps*, **4**, 464 (2021).
19. J. Kriegler, L. Hille, S. Stock, L. Kraft, J. hagemeister, J. B. Habedank, A. jossen, and M. F. Zaeh, *Appl. Energy*, **303**, 117693 (2021).
20. W. Pfleging, *Nanophotonics-berlin*, **7**, 549 (2018).
21. C. L. Cobb and M. Blanco, *J. Power Sources*, **249**, 357 (2014).
22. J. B. Habedank, L. Kraft, A. Rheinfeld, C. Krezdorn, A. Jossen, and M. F. Zaeh, *J. Electrochem. Soc.*, **165**, A1563 (2018).
23. C. Bae, C. K. Erdonmez, J. W. Halloran, and Y. Chiang, *Adv. Mater.*, **25**, 1254 (2013).
24. L. Kraft, J. B. Habedank, A. Frank, A. Rheinfeld, and A. Jossen, *J. Electrochem. Soc.*, **167**, 013506 (2019).
25. L. Hille, L. Xu, J. Keilhofer, S. Stock, J. Kriegler, and M. F. Zaeh, *Electrochemica Acta*, **392**, 139002 (2021).
26. L. Hille, H.-C. Toepper, C. Schriever, J. Kriegler, J. Keilhofer, M. P. Noecker, and M. F. Zae, *J. Electrochem. Soc.*, **169**, 060518 (2022).
27. V. Goel, K.-H. Chen, N. P. Dasgupta, and K. Thornton, *Energy Storage Mater.*, **57**, 44 (2023).
28. A. Shodiev, F. M. Zanotto, J. Yu, M. Chouchane, J. Li, and A. A. Franco, *Energy Storage Mater.*, **49**, 268 (2022).
29. M. G. Berhe, H. G. Oh, S.-K. Park, M. Mondal, and D. Lee, *Mater. Des.*, **231**, 112020 (2023).
30. C. Sauter, R. Zahn, and V. Wood, *J. Electrochem. Soc.*, **167**, 100546 (2020).
31. A. Shodiev, E. Primo, O. Arcelus, M. Chouchane, M. Osenberg, A. Hilger, I. Manke, J. Li, and A. A. Franco, *Energy Storage Mater.*, **38**, 80 (2021).
32. L. Schweighofer, B. Eschelmüller, K. Fröhlich, W. Pfleging, and F. Pichler, *Nanomaterials*, **12**, 9 (2022).
33. V. P. Nemani, S. J. Harris, and K. C. Smith, *J. Electrochem. Soc.*, **162**, A1415 (2015).
34. S. Katoch, S. S. Chauhan, and V. Kumar, *Multimed Tools Appl*, **80**, 8091 (2021).
35. L. Zhang, L. Wang, G. Hinds, C. Lyu, J. Zheng, and J. Li, *J. Power Sources*, **270**, 367 (2014).
36. K. Deb, A. Pratap, S. Agarwal, and T. Meyarivan, *Ieee T Evolut Comput*, **6**, 182 (2002).
37. C. Hwang and K. Yoon, *Multiple Attributes Decision Making Methods And Applications* (Heidelberg)(Springer Berlin) (1981).
38. J. C. Forman, S. J. Moura, J. L. Stein, and H. K. Fathy, *J. Power Sources*, **210**, 263 (2012).
39. P. Kumar and P. Bauer, "Int Power Elect Mot." *14th International Power Electronics and Motion Control Conference, EPE-PEMC* (2010) T9-106-T9-110.
40. Y. Hu, S. Yurkovich, Y. Guezennec, and B. J. Yurkovich, *Control Eng. Pract.*, **17**, 1190 (2009).
41. K. Thirugnanam, E. Reena Joy T. P, M. Singh, and P. Kumar, *Ieee T Energy Conver*, **29**, 332 (2014).
42. A. Brand, Z. Zhang, and R. K. Agarwal, *J. Power Sources*, **247**, 729 (2014).
43. Y. Shen, *AIP Conf. Proc.*, **1955**, 040050 (2018).
44. J. Meng, L. Cai, D.-I. Stroe, G. Luo, X. Sui, and R. Teodorescu, *Energy*, **185**, 1054 (2019).
45. Z. Wang, J. Ma, and L. Zhang, *Ieee Access*, **5**, 21286 (2017).

46. J. Lu, Z. Chen, Y. Yang, and M. Lv, *Ieee Access*, **6**, 20868 (2018).
47. J. Yan, G. Xu, H. Qian, Y. Xu, and Z. Song, *Energies*, **4**, 1178 (2011).
48. C. Liu and L. Liu, *ECS Trans.*, **77**, 257 (2017).
49. N. T. Milas, D. A. Mourtzis, P. I. Giotakos, and E. C. Tatakis, *2020 22nd European Conf Power Electron Appl Epe'20 Ecce Europe, 00, P.1-P.10* (2020).
50. M. Elmehdi and M. Abdelilah, *Proc 2nd Int Conf Netw Information Syst Secur - Niss19, 3* (2019).
51. G. Celli, F. Pilo, G. Monni, and G. G. Soma, *2018 Ieee Int Conf Environ Electr Eng 2018 Ieee Industrial Commer Power Syst Europe Eeeic Cps Europe*, 1 (2018).
52. S. Johnston, D. B. Sulas, and G. F. Kroeger, *2019 IEEE 46th Photovolt. Specialists Conf. PVSC*, **00**, 2753 (2019).
53. A. Schilling, P. Gümbel, M. Möller, F. Kalkan, F. Dietrich, and K. Dröder, *J. Electrochem. Soc.*, **166**, A5163 (2018).
54. A. Gersborg-Hansen, M. P. Bendsøe, and O. Sigmund, *Struct Multidiscip O*, **31**, 251 (2006).
55. A. Bejan, *Int J Heat Mass Tran*, **40**, 799 (1997).
56. Z. Lyu, F. Pourfattah, A. A. A. Arani, A. Asadi, and L. K. Foong, *Sci Rep.*, **10**, 7243 (2020).
57. W. Wechsatol, S. Lorente, and A. Bejan, *Int J Heat Mass Tran*, **45**, 4911 (2002).
58. M. Ebner, D.-W. Chung, R. E. García, and V. Wood, *Adv. Energy mater.*, **4**, 1301278 (2014).
59. F. L. E. Usseglio-Viretta, D. P. Finegan, A. Colclasure, T. M. M. Heenan, D. Abraham, P. Shearing, and K. Smith, *J. Electrochem. Soc.*, **167**, 100513 (2020).
60. K. Jebari and M. Madiaf, *Int. J. Emerg. Sci.*, **4**, 333 (2013).